# Article

# Structure of human telomerase holoenzyme with bound telomeric DNA

George E. Ghanim[1,7], Adam J. Fountain[1,7], Anne-Marie M. van Roon[1,7], Ramya Rangan[2], Rhiju Das[2,3,4], Kathleen Collins[5,6] & Thi Hoang Duong Nguyen[1✉]

Telomerase adds telomeric repeats at chromosome ends to compensate for the telomere loss that is caused by incomplete genome end replication[1]. In humans, telomerase is upregulated during embryogenesis and in cancers, and mutations that compromise the function of telomerase result in disease[2]. A previous structure of human telomerase at a resolution of 8 Å revealed a vertebrate-specific composition and architecture[3], comprising a catalytic core that is flexibly tethered to an H and ACA (hereafter, H/ACA) box ribonucleoprotein (RNP) lobe by telomerase RNA. High-resolution structural information is necessary to develop treatments that can effectively modulate telomerase activity as a therapeutic approach against cancers and disease. Here we used cryo-electron microscopy to determine the structure of human telomerase holoenzyme bound to telomeric DNA at sub-4 Å resolution, which reveals crucial DNA- and RNA-binding interfaces in the active site of telomerase as well as the locations of mutations that alter telomerase activity. We identified a histone H2A–H2B dimer within the holoenzyme that was bound to an essential telomerase RNA motif, which suggests a role for histones in the folding and function of telomerase RNA. Furthermore, this structure of a eukaryotic H/ACA RNP reveals the molecular recognition of conserved RNA and protein motifs, as well as interactions that are crucial for understanding the molecular pathology of many mutations that cause disease. Our findings provide the structural details of the assembly and active site of human telomerase, which paves the way for the development of therapeutic agents that target this enzyme.

In most eukaryotes, telomerase synthesizes telomeric repeats (TTAGGG in humans) at chromosome ends using an integral RNA template within telomerase RNA (known as TER or TR in humans (hereafter, hTR)) and telomerase reverse transcriptase (TERT)[4]. As with other polymerases, the synthesis by telomerase of a single telomeric repeat involves repetitive cycles of nucleotide addition[5]. Telomerase has a unique ability to synthesize several telomeric repeats with each binding event, which is known as repeat addition processivity[6]. Despite numerous structural characterizations, the structural determinants of the activity of human telomerase remain poorly understood owing to the lack of a high-resolution structure of human TERT. Vertebrate telomerase RNAs contain a 3' H/ACA domain that is essential for the biogenesis and regulation of telomerase RNP[3,7]. This H/ACA domain is shared with an evolutionarily conserved family of noncoding RNA that includes small nucleolar RNA and small Cajal body RNA, which function as guides for site-specific pseudouridylation of ribosomal and spliceosomal RNAs[8]. Archaeal ACA RNAs contain a single RNA hairpin with a 3' ACA motif, whereas eukaryotic H/ACA RNAs consist of two RNA hairpins that are hinged by the H box and flanked by an ACA motif at the 3' end. Each RNA hairpin associates with a heterotetramer of dyskerin, NOP10, NHP2 and

GAR1. Mutations in the H/ACA RNP are associated with telomeropathies—notably, dyskeratosis congenita and Hoyeraal–Hreidarsson syndrome[9], which affect highly proliferating tissues and result in pulmonary and bone marrow abnormalities[2]. High-resolution structural information of these H/ACA RNPs is currently limited to single-hairpin archaeal and yeast structures[10,11], which cannot rationalize many of these mutations.

## Structure determination

We collected 43,639 cryo-electron microscopy (cryo-EM) micrographs on a Gatan K3 detector, and performed signal subtraction combined with extensive classification[12] to overcome the conformational flexibility of the complex (Extended Data Fig. 1). The resulting reconstructions, at resolutions of 3.4 Å and 3.8 Å for the H/ACA RNP and the catalytic core, respectively, enabled us to build de novo atomic models for each lobe (Fig. 1a, Extended Data Figs. 2a–d, 3a–p, 4b–l, Extended Data Tables 1, 2, Supplementary Data 1). We performed global classification and refinement to obtain reconstructions for the whole telomerase complex (Extended Data Figs. 1, 2e, f). Multibody refinement[13] revealed that

[1]Medical Research Council Laboratory of Molecular Biology, Cambridge, UK. [2]Biophysics Program, Stanford University, Stanford, CA, USA. [3]Department of Biochemistry, Stanford University, Stanford, CA, USA. [4]Department of Physics, Stanford University, Stanford, CA, USA. [5]Department of Molecular and Cell Biology, University of California, Berkeley, CA, USA. [6]California Institute for Quantitative Biology (QB3), University of California, Berkeley, CA, USA. [7]These authors contributed equally: George E. Ghanim, Adam J. Fountain, Anne-Marie M. van Roon. ✉e-mail: knguyen@mrc-lmb.cam.ac.uk
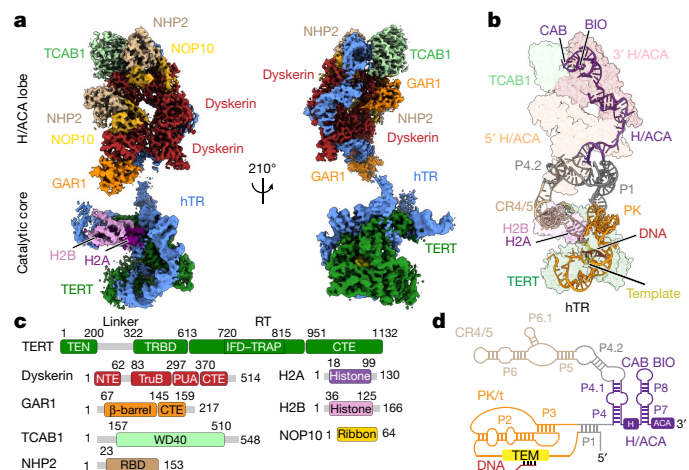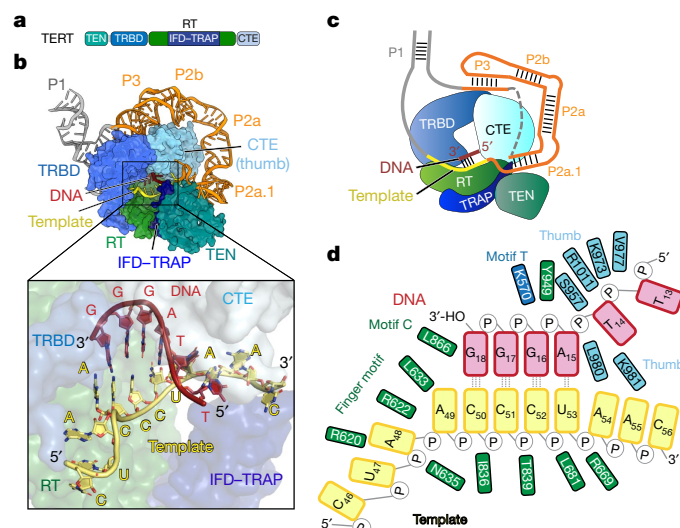
**Fig. 1 | Cryo-EM structure of human telomerase holoenzyme. a**, Front (left) and back (right) views of the composite cryo-EM maps of the catalytic core and the H/ACA lobe at 3.8 Å and 3.4 Å, respectively, with subunits coloured as indicated. **b**, Front view of the structure in which hTR and the DNA substrate are highlighted. **c**, Domain architectures of protein subunits. TEN, telomerase essential N-terminal domain; TRBD, telomerase RNA-binding domain; CTE, C-terminal extension; NTE, N-terminal extension; RT, reverse transcriptase; TruB, tRNA pseudouridine synthase B-like domain; WD40, Trp-Asp 40 repeat domain; RBD, RNA-binding domain. **d**, Secondary structure of hTR and the DNA substrate (Extended Data Fig. 4a). TEM, template.



**Fig. 2 | Catalytic core of human telomerase. a**, Domain architecture of TERT. This domain colour scheme is used throughout the Article, unless otherwise stated. **b**, TERT structure with the PK/t domain of hTR and the DNA substrate. The inset shows a close-up view of the DNA substrate–RNA template duplex in the active site of TERT (Extended Data Fig. 4d). **c**, Cartoon of TERT domains, PK/t domain of hTR and the DNA substrate. **d**, Schematic of the DNA–RNA duplex observed in our structure and interactions with TERT residues (Extended Data Fig. 6d–f).

the two lobes adopted several conformations relative to each other (Extended Data Fig. 5a–c). We docked the atomic models of the two lobes into these whole telomerase reconstructions, and combined this with DRRAFTER modelling[14] of the RNA linkers between the two lobes (Extended Data Fig. 5d, e). The resulting atomic model for the human telomerase holoenzyme consists of hTR, a telomeric DNA substrate and 12 protein subunits (TERT, TCAB1, a histone H2A–H2B dimer and two copies of the H/ACA heterotetramer) (Fig. 1a–d, Supplementary Data 2, 3). TERT and histone H2A–H2B form the catalytic core with the pseudoknot and template (hereafter, PK/t) and conserved regions 4 and 5 (hereafter, CR4/5) of hTR; both PK/t and CR4/5 are essential for activity[15] (Fig. 1a–d). The remaining subunits associate with the H/ACA domain of hTR to form the H/ACA lobe (Fig. 1a–d). The catalytic core and H/ACA lobe are connected by the P1 and P4.2 stems of hTR (Fig. 1b, d, Extended Data Fig. 5d, e).

## Active site of telomerase

TERT has four domains: a telomerase essential N-terminal (TEN) domain, a telomerase RNA-binding domain (TRBD), a reverse transcriptase domain and a C-terminal extension (CTE) (which is also known as the thumb domain) (Figs. 1c, 2a–c). As was first visualized in *Tetrahymena* TERT[16], the reverse transcriptase domain includes an insertion in the fingers subdomain (known as IFD–TRAP) (Extended Data Fig. 6a, b). In the catalytic core, the PK/t domain of hTR (Fig. 1d) encircles the domains of TERT, forming extensive interactions—mostly through the RNA backbone (Fig. 2b, c). The DNA–RNA duplex is held in the active site (Fig. 2b, c) by interactions with conserved motifs of TERT (Extended Data Figs. 3b, 4d, 6a, b). We observed density for the full 3′ TTAGGG telomeric repeat of the DNA substrate, which contacts residues in motif T (K570), motif C (L866), the thumb loop (S957), the thumb helix (residues 970 to 988), Y949 and R1011 (Fig. 2d, Extended Data Figs. 4e, 6a, b, d). Previous studies have shown that the K570E mutant is severely defective in nucleotide addition processivity, and that mutations affecting thumb residues L958, L980 and K981 lead to reductions in repeat addition processivity[17,18]. The L813Y substitution in *Tetrahymena* TERT (equivalent to L866 in human TERT) increases repeat addition processivity, and this residue

has previously been proposed to bind DNA[19]. Our structure suggests that these residues indicated above are critical for stabilizing the DNA substrate in the active site of telomerase. The defects in nucleotide and repeat addition processivity that are induced by these mutations probably result from premature dissociation of the substrate from the active site during repeat synthesis.

The RNA template is embedded within the reverse transcriptase domain (Extended Data Fig. 6e). Although the DNA substrate could theoretically form up to six base pairs with the RNA template, we observed only four base pairs at the AGGG 3′ end of the substrate (Fig. 2b, d, Extended Data Figs. 4d, 6c). The preceding TT nucleotides are split away from the template by the CTE domain (Fig. 2b, d). The template base A49 is positioned to base-pair with an incoming dTTP nucleotide, and the 3′ hydroxyl of the DNA substrate points towards the catalytic triad (D712, D868 and D869)[5] (Extended Data Figs. 3b, 6f). Residue R622 from the finger motif acts as a ratchet to separate A48 from A49, thereby allowing only one template base into the active site at a time (Fig. 2d, Extended Data Fig. 6f). Residues from the reverse transcriptase finger (R631), motif B (Q833) and Y717 are in the vicinity of the vacant nucleotide site (Extended Data Fig. 6f). Previous structures of the *Tribolium* TERT suggest a role for Y256 (equivalent to Y717 in human TERT) as a steric gate that discriminates rNTPs from dNTPs and allows only dNTPs to be incorporated[20]. *Tetrahymena* TERT loses its dNTP and rNTP selectivity when mutated at the equivalent tyrosine (Y623A)[21]. We modelled a dTTP nucleotide[22] that would base-pair with the template A49 in the vacant nucleotide site. A hydroxyl group at the ribose C2 would clash with the side chain of Y717, which suggests that the role for Y717 in human TERT is similar to that of Y256 in *Tribolium* TERT or Y623 in *Tetrahymena* TERT (Extended Data Fig. 6g).

## TERT interactions with the CR4/5 domain of hTR

The CR4/5 domain encompasses the P5, P6 and P6.1 regions of hTR (Fig. 1d), which connect as a three-way junction (Fig. 3a). The P6.1 hairpin is highly conserved in vertebrates, and its duplex length and the two conserved loop nucleotides U307 and G309 are essential for
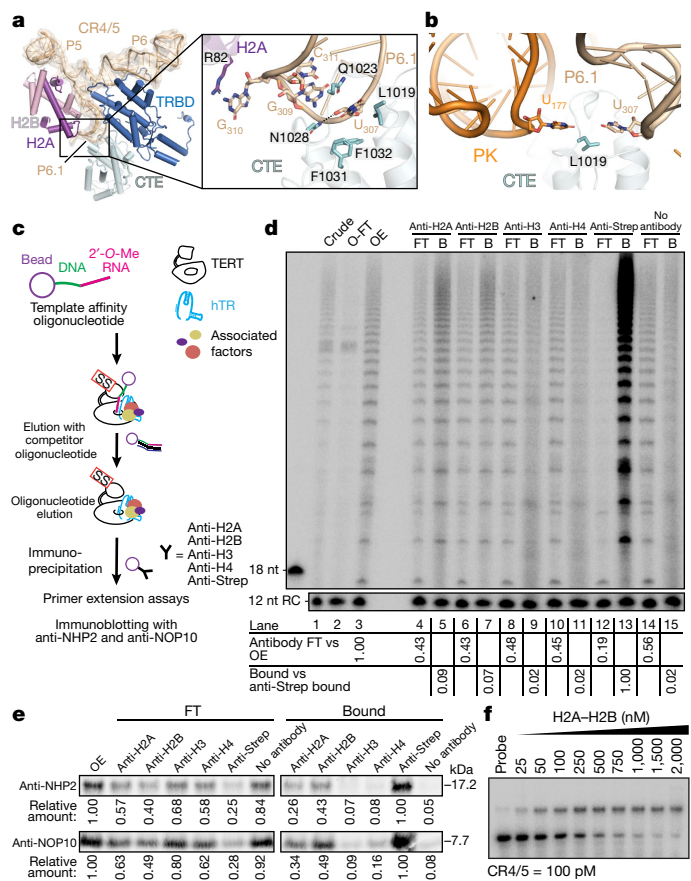
**Fig. 3 | CR4/5 interactions with TERT and histone H2A–H2B subunits.**
**a**, CR4/5 domain of hTR and its interaction with the TRBD and CTE domains of TERT, and the histone H2A–H2B dimer. The inset provides a close-up view to highlight the recognition of the P6.1 apical loop by TERT and H2A (Extended Data Fig. 4g, h). **b**, The close proximity of PK (orange) and the P6.1 stem loop (wheat) (Extended Data Fig. 4i). **c**, Schematic of 2′-O-methyl oligonucleotide purification coupled with immunoprecipitation to confirm the presence of histone H2A–H2B in human telomerase structure. SS, twin Strep tag. **d**, Activity assay results of immunoprecipitation experiments, performed as outlined in **c**. Crude, input lysate; O-FT, flow-through from oligonucleotide purification; OE, elution from oligonucleotide purification; FT, flow-through from immunoprecipitation with each set of antibodies; B, bound sample on beads from immunoprecipitation with each set of antibodies; 12 nt RC, 12-nucleotide recovery control; 18 nt, 18-nucleotide marker. We performed two separate quantifications. Each FT activity is quantified relative to input (OE) activity. Each bound activity is quantified relative to an anti-Strep immunoprecipitation positive control. All quantifications are normalized to the signal of the recovery control. **e**, Immunoblot analyses of immunoprecipitation experiments, performed as outlined in **c**. Each fraction was immunoblotted with NHP2 antibody and NOP10 antibody. Signal from each flow-through fraction (FT) was quantified relative to the input (OE) signal. Signal from each bound fraction (bound) was quantified relative to the anti-Strep immunoprecipitation signal. **f**, Native electrophoretic mobility shift assays showing titration of purified histone H2A–H2B against ³²P-end-labelled CR4/5 RNA. Quantification is shown in Extended Data Fig. 7k. Experiments in **d**–**f** were done in three technical replicates (Supplementary Figs. 1, 2).

telomerase activity[23,24]. U307 flips out into a hydrophobic pocket of the CTE, and interacts with N1028 (Fig. 3a, Extended Data Fig. 4h). G309 is coordinated by Q1023 and base-stacks with C311 (Fig. 3a). P6.1 is also in close proximity to the P3 stem of the PK/t domain. Notably, both the bulged U177 in P3 and the flipped-out U307 of P6.1 interact with L1019 (Fig. 3b, Extended Data Fig. 4i). P5 makes no interactions with TERT, which explains why it is not required for reconstituting telomerase activity in lysates[25]. Although the CR4/5 domain does not directly

contact the active site of TERT, our structure suggests that—together with PK/t—it ensures the correct positioning of TERT domains, which is important for the catalytic activity of telomerase.

## Histones H2A and H2B are telomerase subunits

During 3D classification of the catalytic core, most classes contained an unaccounted-for density bound to CR4/5 (Extended Data Figs. 1, 7a). This density was unmodelled in the previous map[3] (Extended Data Fig. 7b). Aided by the improved resolution in the structure discussed here, we performed a molecular replacement search against the BAL-BES database[26] and obtained histone H2B (Protein Data Bank code (PDB) 1KX5)[27] as the top hit. The fitting of a histone H2A–H2B dimer extracted from a nucleosome structure accounted for the entire density (Extended Data Figs. 3e–h, 7c). Mass spectrometry analyses of purified telomerase showed the presence of histones H2A, H2B, H3 and H4 (Supplementary Data 4).

As an independent test of this association, we overexpressed telomerase using a twin Strep-tagged TERT construct and performed 2′-O-methyl oligonucleotide purification to enrich for hTR[28] (Fig. 3c). Immunoblotting indicated the presence of histones H2B, H2A, H3 and H4 in oligonucleotide affinity-purified telomerase RNP (Extended Data Fig. 7g). We made similar observations using endogenous telomerase purified from HEK 293T cells (Extended Data Fig. 7h).

To test whether histone-containing telomerase RNPs are active for the synthesis of telomeric repeats, we further purified telomerase RNPs using antibodies against histones or the Strep tag and performed telomerase activity assays and immunoblotting (Fig. 3d, e). Immunoprecipitation with histone H2A or H2B antibodies purified telomerase activity and holoenzyme components (Fig. 3d lanes 5 and 7, e), whereas histone H3 and H4 antibodies recovered relatively less telomerase activity and components (Fig. 3d lanes 9 and 11, e). Compared to TERT Strep tag immunoprecipitation (lane 13 in Fig. 3d), a smaller fraction of input telomerase activity was recovered in association with histones H2A and H2B (lanes 5 and 7 in Fig. 3d), consistent with a subset of telomerase holoenzyme particles having homogenous density for the histone H2A–H2B dimer. Histones H3 and H4—which were not observed in the density of analysed particle classes—are either absent or associated with the holoenzyme, but are too flexible to contribute to observable densities.

The histone H2A–H2B dimer binds to the three-way junction across the P5 and P6.1 stems, using the same positively charged histone H2A–H2B surface that binds nucleosomal DNA (Fig. 3a, Extended Data Fig. 7d, e). Consistent with our model, purified recombinant human histone H2A–H2B dimer bound CR4/5 in native gel assays (Fig. 3f, Extended Data Fig. 7f, k). Previous work has emphasized that CR4/5 alone adopts heterogeneous conformations[29]. In holoenzyme particles, CR4/5 adopts a more homogenous conformation. Together, these findings suggest that the histone H2A–H2B heterodimer may act to stabilize and/or position the CR4/5 fold during telomerase RNP assembly in cells. This would explain why active human telomerase is not readily reconstituted from purified TERT and hTR, but can be assembled by co-expression of TERT and hTR in vivo.

## The H/ACA RNP structure

The structure of a complete eukaryotic H/ACA RNP presented in this Article reveals numerous molecular interactions that were not possible to infer from previous single-hairpin archaeal and yeast RNP structures[10,11]. The double-hairpin H/ACA RNA scaffolds the assembly of two copies each of dyskerin, NHP2, NOP10 and GAR1, one on each hairpin (Fig. 4a, Extended Data Fig. 8a, b). For clarity, we describe the components of the assemblies bound to the 5′ and 3′ hairpins as 5′ and 3′, respectively (Fig. 4a).

The conserved H and ACA boxes are brought into close proximity to one another by the two dyskerin molecules (Fig. 4a, Extended Data

# Article
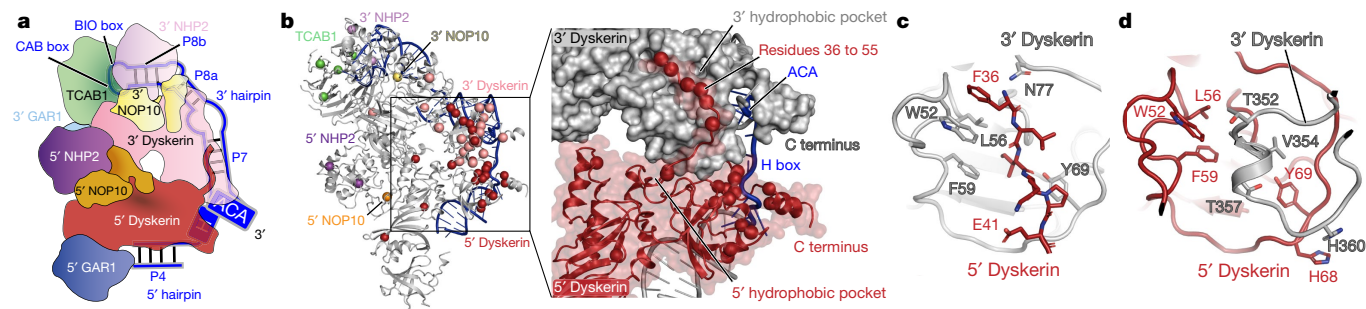


Fig. 4 | H/ACA RNP structure and mutations linked with disease in humans. a, Schematic of the H/ACA RNP, showing hTR interactions with the H/ACA proteins. b, Overall structure of the H/ACA RNP. Mutations that are associated with dyskeratosis congenita or Hoyeraal–Hreidarsson syndrome are highlighted as spheres[9]. Inset, close-up view of the disease mutation hotspot, which lies at the interface between the two dyskerin molecules. c, The hydrophobic pocket of 3′ dyskerin, which accommodates the N-terminal extension of the 5′ dyskerin (Extended Data Fig. 3m). d, The hydrophobic pocket of 5′ dyskerin, which accommodates helix 352–357 of 3′ dyskerin (Extended Data Fig. 3n).

Figs. 3p, 4k, 8a, c). The AGA motif of the H box (ANANNAA; underlining denotes the motif) and the ACA box form similar interactions with the 5′ and 3′ dyskerin molecules, respectively (Extended Data Fig. 8c). The conserved A377 of the H box and C447 of the ACA box form van der Waals and stacking interactions with each other, and with the 3′ dyskerin (Extended Data Figs. 4k, 8c). These cross-hairpin interactions distinguish eukaryotic H/ACA two-hairpin RNPs from archaeal ACA single-hairpin RNPs.

The P8b hairpin (Fig. 4a, Extended Data Fig. 8a) makes unique contributions to the cellular accumulation and localization of hTR[30,31]. The apical hairpin loop contains two motifs: a conserved ugAG sequence (the CAB box), which binds the Cajal body localization factor TCAB1[32–34]; and a biogenesis-promoting (BIO) box that enhances hTR 3′ hairpin assembly as a H/ACA RNP[31] (Extended Data Figs. 3o, 8b, d). Of note, the CAB box is recognized by both TCAB1 and NHP2 (Fig. 4a, Extended Data Figs. 3o, 8d). Loop G412 and G414 form π-stacking interactions, supported by the coordination of R387 and a number of hydrophobic residues of TCAB1 to G414 (Extended Data Figs. 4l, 8d). This purine–purine stacking positions G414 and A413 for interactions with TCAB1. A413 and G414 have previously been shown to promote Cajal body localization, and the G414C substitution is sufficient to abolish TCAB1 association with telomerase holoenzyme[32]. The G414C substitution could destabilize this stacking structure and therefore the interaction between hTR and TCAB1.

The positioning of the 3′ loop region of the CAB box is assisted by the BIO box. The conserved U418 within the BIO box flips out and interacts with K111 and L86 of NHP2 (Extended Data Fig. 8d). Despite being required for Cajal body localization, the CAB box is dispensable for hTR accumulation[30,35]. However, a U418C substitution in the BIO box strongly disrupts hTR accumulation[31]. The observed interaction between the BIO box and NHP2 explains the enhanced affinity of the telomerase 3′ H/ACA hairpin for H/ACA proteins, and suggests that NHP2 binding to the P8b hairpin could stabilize or remodel the loop for TCAB1 binding.

## Disease mutations in the H/ACA RNP

We modelled parts of the N and C termini of both dyskerin molecules that were either unresolved or adopted different conformations in previous structures[10,11]. A 5′ dyskerin N-terminal extension (residues 36 to 55) sits in the 3′ dyskerin hydrophobic pocket formed by the N-terminal region and the pseudouridine synthase and archaeosine transglycosylase (PUA) domain (Fig. 4b, c, Extended Data Fig. 3m). The equivalent hydrophobic pocket of the 5′ dyskerin subunit seats a helix (residues 352 to 357) of the 3′ dyskerin (Fig. 4b, d, Extended Data Fig. 3n). The N-terminal extension and this hydrophobic pocket of dyskerin contain most of the mutations that are associated with dyskeratosis congenita

or Hoyeraal–Hreidarsson syndrome[9] (Fig. 4b). These mutations probably disrupt the reciprocal dyskerin–dyskerin interactions, and thus telomerase RNP assembly. Most of the remaining mutations that are associated with disease map to other important protein–protein and protein–RNA interfaces (Fig. 4b). In light of our structure, assembly of native telomerase H/ACA RNP would rely on a combination of the cross-hairpin dyskerin interactions and an increased H/ACA protein affinity for the 3′ H/ACA RNA hairpin that is afforded by NHP2.

## Discussion

The structure reported in this Article provides not only insight into the active site of human telomerase, but also clues about the requirements for RNP biogenesis and a role for histone proteins beyond the nucleosome.

The synthesis of multiple repeats necessitates that human telomerase undergoes a complex catalytic cycle that involves the translocation of the nascent DNA product and its realignment with the template region of hTR[17,36] (Extended Data Fig. 6c). After dissociation from the template, the nascent DNA product is retained to enable rebinding of the DNA 3′ end to the alignment region of the template (Extended Data Fig. 6c, l). The non-template single-stranded DNA-binding interface has been described as an 'anchor point' during catalysis that allows for retention of the DNA product[17,37]. In our structure, the enzyme is bound to a 3′ TTAGGG repeat, poised to bind an incoming dNTP (Extended Data Fig. 6c). The structure reveals an extensive DNA-binding surface around the active site that is predominantly formed by the T motif and the CTE domain (Fig. 2d, Extended Data Fig. 6d). Our structure also shows a positively charged surface at the interface between human IFD–TRAP subdomain and the TEN domain of TERT that could potentially guide DNA away from the active site (Extended Data Fig. 6h–j) and provide an anchor point for the DNA substrate (Extended Data Fig. 6l).

In human cells, telomerase is recruited to telomeres by TPP1–POT1 (which are components of the shelterin complex) through interactions between TPP1 and the TEN domain of TERT[38–41]. We modelled TPP1–POT1 bound to the human TEN domain using the analogous *Tetrahymena* p50–TEB complex[16]. The role of the p50–TEB complex in telomerase recruitment and activation in *Tetrahymena* has previously been proposed to parallel that of TPP1–POT1 in human[42,43]. The proposed DNA path would bring the product DNA close to the single-stranded DNA-binding domains of POT1 in this TPP1–POT1 model (Extended Data Fig. 6i–k).

We discovered a role for the histone H2A–H2B heterodimer as an RNA-binding factor for the CR4/5 domain of hTR. Our structure suggests that histone H2A–H2B functions in human telomerase to perform a role similar to that of the La-family *Tetrahymena* telomerase holoenzyme protein p65[44]. p65 binds to *Tetrahymena* stem loop 4–which has

structural placement somewhat similar to that of the P6.1 stem loop in CR4/5 in the telomerase catalytic core—to stabilize a TER conformational change that promotes TERT–TER interactions[45] (Extended Data Fig. 7i, j). Superimposition of the histone octamer with flexible tails removed on histone H2A–H2B in the telomerase catalytic core results in very little clashing, and therefore may be compatible with histone H3–H4 binding (Extended Data Fig. 7l). Telomerase has previously been proposed to associate with the replication fork to account for replication coupling of telomerase action at telomeres[46,47]. After replication fork passage, histone H3–H4 tetramers are deposited on the daughter DNA free of histone H2A–H2B[48]. It is tempting to speculate that the histone H2A–H2B heterodimer within the telomerase holoenzyme has a role in recruiting telomerase to chromosome ends specifically after replication, through interactions with replication-coupled deposition of histone H3–H4 tetramers. Furthermore, histone H2A–H2B availability for hTR interaction could regulate the assembly or telomere recruitment of active telomerase holoenzyme across the cell cycle.

## Online content

Any methods, additional references, Nature Research reporting summaries, source data, extended data, supplementary information, acknowledgements, peer review information; details of author contributions and competing interests; and statements of data and code availability are available at https://doi.org/10.1038/s41586-021-03415-4.

1. Levy, M. Z., Allsopp, R. C., Futcher, A. B., Greider, C. W. & Harley, C. B. Telomere end-replication problem and cell aging. *J. Mol. Biol.* **225**, 951–960 (1992).
2. Shay, J. W. Role of telomeres and telomerase in aging and cancer. *Cancer Discov.* **6**, 584–593 (2016).
3. Nguyen, T. H. D. et al. Cryo-EM structure of substrate-bound human telomerase holoenzyme. *Nature* **557**, 190–195 (2018).
4. Blackburn, E. H. & Collins, K. Telomerase: an RNP enzyme synthesizes DNA. *Cold Spring Harb. Perspect. Biol.* **3**, a003558 (2011).
5. Lingner, J. et al. Reverse transcriptase motifs in the catalytic subunit of telomerase. *Science* **276**, 561–567 (1997).
6. Wu, R. A., Upton, H. E., Vogan, J. M. & Collins, K. Telomerase mechanism of telomere synthesis. *Annu. Rev. Biochem.* **86**, 439–460 (2017).
7. MacNeil, D. E., Bensoussan, H. J. & Autexier, C. Telomerase regulation from beginning to the end. *Genes* **7**, 64 (2016).
8. Yu, Y.-T. & Meier, U. T. RNA-guided isomerization of uridine to pseudouridine—pseudouridylation. *RNA Biol.* **11**, 1483–1494 (2014).
9. Sarek, G., Marzec, P., Margalef, P. & Boulton, S. J. Molecular basis of telomere dysfunction in human genetic diseases. *Nat. Struct. Mol. Biol.* **22**, 867–874 (2015).
10. Li, L. & Ye, K. Crystal structure of an H/ACA box ribonucleoprotein particle. *Nature* **443**, 302–307 (2006).
11. Li, S. et al. Reconstitution and structural analysis of the yeast box H/ACA RNA-guided pseudouridine synthase. *Genes Dev.* **25**, 2409–2421 (2011).
12. Bai, X.-C., Rajendra, E., Yang, G., Shi, Y. & Scheres, S. H. W. Sampling the conformational space of the catalytic subunit of human γ-secretase. *eLife* **4**, e11182 (2015).
13. Nakane, T., Kimanius, D., Lindahl, E. & Scheres, S. H. W. Characterisation of molecular motions in cryo-EM single-particle data by multi-body refinement in RELION. *eLife* **7**, e36861 (2018).
14. Kappel, K. et al. De novo computational RNA modeling into cryo-EM maps of large ribonucleoprotein complexes. *Nat. Methods* **15**, 947–954 (2018).
15. Podlevsky, J. D. & Chen, J. J. Evolutionary perspectives of telomerase RNA structure and function. *RNA Biol.* **13**, 720–732 (2016).
16. Jiang, J. et al. Structure of telomerase with telomeric DNA. *Cell* **173**, 1179–1190 (2018).
17. Wu, R. A., Tam, J. & Collins, K. DNA-binding determinants and cellular thresholds for human telomerase repeat addition processivity. *EMBO J.* **36**, 1908–1927 (2017).
18. Qi, X. et al. RNA/DNA hybrid binding affinity determines telomerase template-translocation efficiency. *EMBO J.* **31**, 150–161 (2012).
19. Bryan, T. M., Goodrich, K. J. & Cech, T. R. A mutant of *Tetrahymena* telomerase reverse transcriptase with increased processivity. *J. Biol. Chem.* **275**, 24199–24207 (2000).
20. Schaich, M. A. et al. Mechanisms of nucleotide selection by telomerase. *eLife* **9**, e55438 (2020).
21. Miller, M. C., Liu, J. K. & Collins, K. Template definition by *Tetrahymena* telomerase reverse transcriptase. *EMBO J.* **19**, 4412–4422 (2000).
22. Nair, D. T., Johnson, R. E., Prakash, S., Prakash, L. & Aggarwal, A. K. Replication by human DNA polymerase-ι occurs by Hoogsteen base-pairing. *Nature* **430**, 377–380 (2004).
23. Chen, J. L., Opperman, K. K. & Greider, C. W. A critical stem-loop structure in the CR4–CR5 domain of mammalian telomerase RNA. *Nucleic Acids Res.* **30**, 592–597 (2002).
24. Robart, A. R. & Collins, K. Investigation of human telomerase holoenzyme assembly, activity, and processivity using disease-linked subunit variants. *J. Biol. Chem.* **285**, 4375–4386 (2010).
25. Kim, N. K., Theimer, C. A., Mitchell, J. R., Collins, K. & Feigon, J. Effect of pseudouridylation on the structure and activity of the catalytically essential P6.1 hairpin in human telomerase RNA. *Nucleic Acids Res.* **38**, 6746–6756 (2010).
26. Long, F., Vagin, A. A., Young, P. & Murshudov, G. N. BALBES: a molecular-replacement pipeline. *Acta Crystallogr. D* **64**, 125–132 (2008).
27. Davey, C. A., Sargent, D. F., Luger, K., Maeder, A. W. & Richmond, T. J. Solvent mediated interactions in the structure of the nucleosome core particle at 1.9 a resolution. *J. Mol. Biol.* **319**, 1097–1113 (2002).
28. Schnapp, G., Rodi, H.-P., Rettig, W. J., Schnapp, A. & Damm, K. One-step affinity purification protocol for human telomerase. *Nucleic Acids Res.* **26**, 3311–3313 (1998).
29. Palka, C., Forino, N. M., Hentschel, J., Das, R. & Stone, M. D. Folding heterogeneity in the essential human telomerase RNA three-way junction. *RNA* **26**, 1787–1800 (2020).
30. Fu, D. & Collins, K. Distinct biogenesis pathways for human telomerase RNA and H/ACA small nucleolar RNAs. *Mol. Cell* **11**, 1361–1372 (2003).
31. Egan, E. D. & Collins, K. An enhanced H/ACA RNP assembly mechanism for human telomerase RNA. *Mol. Cell. Biol.* **32**, 2428–2439 (2012).
32. Tycowski, K. T., Shu, M. D., Kukoyi, A. & Steitz, J. A. A conserved WD40 protein binds the Cajal body localization signal of scaRNP particles. *Mol. Cell* **34**, 47–57 (2009).
33. Venteicher, A. S. et al. A human telomerase holoenzyme protein required for Cajal body localization and telomere synthesis. *Science* **323**, 644–648 (2009).
34. Theimer, C. A. et al. Structural and functional characterization of human telomerase RNA processing and cajal body localization signals. *Mol. Cell* **27**, 869–881 (2007).
35. Jády, B. E., Bertrand, E. & Kiss, T. Human telomerase RNA and box H/ACA scaRNAs share a common Cajal body-specific localization signal. *J. Cell Biol.* **164**, 647–652 (2004).
36. Parks, J. W. & Stone, M. D. Coordinated DNA dynamics during the human telomerase catalytic cycle. *Nat. Commun.* **5**, 4146 (2014).
37. Patrick, E. M., Slivka, J. D., Payne, B., Comstock, M. J. & Schmidt, J. C. Observation of processive telomerase catalysis using high-resolution optical tweezers. *Nat. Chem. Biol.* **16**, 801–809 (2020).
38. Nandakumar, J. et al. The TEL patch of telomere protein TPP1 mediates telomerase recruitment and processivity. *Nature* **492**, 285–289 (2012).
39. Latrick, C. M. & Cech, T. R. POT1–TPP1 enhances telomerase processivity by slowing primer dissociation and aiding translocation. *EMBO J.* **29**, 924–933 (2010).
40. Zhong, F. L. et al. TPP1 OB-fold domain controls telomere maintenance by recruiting telomerase to chromosome ends. *Cell* **150**, 481–494 (2012).
41. Sexton, A. N., Youmans, D. T. & Collins, K. Specificity requirements for human telomere protein interaction with telomerase holoenzyme. *J. Biol. Chem.* **287**, 34455–34464 (2012).
42. Upton, H. E., Hong, K. & Collins, K. Direct single-stranded DNA binding by Teb1 mediates the recruitment of *Tetrahymena thermophila* telomerase to telomeres. *Mol. Cell. Biol.* **34**, 4200–4212 (2014).
43. Jiang, J. et al. Structure of *Tetrahymena* telomerase reveals previously unknown subunits, functions, and interactions. *Science* **350**, aab4070 (2015).
44. Witkin, K. L. & Collins, K. Holoenzyme proteins required for the physiological assembly and activity of telomerase. *Genes Dev.* **18**, 1107–1118 (2004).
45. Stone, M. D. et al. Stepwise protein-mediated RNA folding directs assembly of telomerase ribonucleoprotein. *Nature* **446**, 458–461 (2007).
46. Greider, C. W. Regulating telomere length from the inside out: the replication fork model. *Genes Dev.* **30**, 1483–1491 (2016).
47. Margalef, P. et al. Stabilization of reversed replication forks by telomerase drives telomere catastrophe. *Cell* **172**, 439–453 (2018).
48. Sauer, P. V. et al. Mechanistic insights into histone deposition and nucleosome assembly by the chromatin assembly factor-1. *Nucleic Acids Res.* **46**, 9907–9917 (2018).

# Article

## Methods

No statistical methods were used to predetermine sample size. The experiments were not randomized, and investigators were not blinded to allocation during experiments and outcome assessment.

### Telomerase purification

We reconstituted human telomerase in HEK 293T cells by co-expression of a TERT expression plasmid (pcDNA 3.1-ZZ-TEV-twin Strep-TERT or pcDNA 3.1-twin Strep-TERT) and pcDNA 3.1-U3-hTR-HDV. TEV is a tobacco etch virus protease cleavage site, and HDV is the hepatitis delta virus ribozyme. The human telomerase–DNA substrate ($T_{12}T_2AG_3$) complex used for cryo-EM was purified as previously described[3]. In brief, whole-cell extracts were prepared from transfected HEK 293T cells by three freeze–thaw cycles. Extracts from 120–160 plates of cells were incubated with streptavidin agarose resin (Sigma-Aldrich) prebound to a 5′-biotinylated 2′-O-methyl oligonucleotide at room temperature for 3 h. The resin was then washed with wash buffer (20 mM HEPES NaOH pH 8.0, 150 mM NaCl, 2 mM MgCl$_2$, 0.2 mM EGTA, 10% glycerol, 0.1% Igepal CA-630, 1 mM DTT) and eluted with a competitor oligonucleotide. The eluate was incubated with MagStrep XT resin (IBA LifeSciences) overnight at 4 °C. The resin was washed with wash buffer and eluted in batch with biotin elution buffer (100 mM Tris HCl pH 8.0, 150 mM NaCl, 1 mM EDTA, 5–10 mM biotin, 2 mM MgCl$_2$, 0.1% Igepal CA-630, 10% glycerol, 1 mM DTT). The complex for structural determination has a ZZ-TEV-twin Strep tag on TERT. For the histone experiments, we used a twin Strep-TERT construct to avoid binding of the ZZ tag on IgG sepharose. Endogenous telomerase was purified from whole-cell extracts prepared from HEK 293T cells using 2′-O-methyl oligonucleotide purification. HEK 293T cell lines were obtained from ATCC (ATCC CRL-3216) and exhibited the expected morphology and growth. They have not been authenticated or tested for mycoplasma recently.

### Mass spectrometry

Purified telomerase was analysed by tandem mass spectrometry. The Supplementary Data 4 file shows full mass spectrometry results.

### Histone immunoprecipitation

Whole-cell extract from HEK 293T cells transfected with twin Strep-TERT and hTR expression constructs was subjected to 2′-O-methyl oligonucleotide purification using a 5′-biotinylated 2′-O-methyl oligonucleotide, which can hybridize with hTR template region as described in 'Telomerase purification section'[28,49]. The sample was eluted using a competitor oligonucleotide. Twenty-five µl magnetic protein A/G sepharose beads (Pierce), prebound to anti-H2A, anti-H2B, anti-H3, anti-H4 and anti-Strep or with no antibody (negative control), were incubated with 100 µl eluate overnight at 4 °C. All histone antibodies used were chromatin immunoprecipitation (ChIP) grade. The flow through was collected for western blot (15 µl) and activity assays (5 µl). The beads were washed three times with wash buffer (20 mM HEPES NaOH pH 8.0, 150 mM NaCl, 2 mM MgCl$_2$, 0.2 mM EGTA, 10% glycerol, 0.1% Igepal CA-630, 1 mM DTT) and resuspended in wash buffer. Five per cent or 25% of the resuspended beads were subjected to telomerase activity assays, and 25% of the beads were boiled in SDS loading buffer for SDS–PAGE and immunoblotting.

### Telomerase activity assays

Telomerase primer extension assays were performed in 20-µl reactions containing 50 mM Tris-acetate pH 8.0, 4 mM MgCl$_2$, 5 mM DTT, 250 µM dTTP, 250 µM dATP, 5 µM unlabelled dGTP, 0.1 µM α-$^{32}$P dGTP (3,000 Ci mmol$^{-1}$, 10 mCi ml$^{-1}$) (Perkin Elmer), 500 nM ($T_2AG_3$)$_3$. The reactions were performed at 30 °C for 40 min, stopped with 50 mM Tris HCl pH 7.5, 20 mM EDTA, 0.2% SDS, extracted with phenol:chloroform:isoamyl alcohol and precipitated with ethanol and a 12-nt $^{32}$P-labelled ($T_2AG_3$)$_2$

oligonucleotide. The products were resolved on a 10.5% denaturing polyacrylamide TBE gel, which was dried and exposed to a phosphorimager screen. The screen was scanned using an Amersham Typhoon Biomolecular Imager (Cytiva). Bands were quantified using ImageQuant (Cytiva).

### Immunoblotting

Samples were resolved on a 4–12% Bis-Tris SDS–PAGE gels and transferred onto a nitrocellulose membrane. The membrane was blocked with 5% non-fat milk in phosphate saline buffer (PBS) supplemented with 0.1% Tween-20 (PBST) for 1 h and incubated with primary antibodies overnight at 4 °C. The membrane was then washed with PBST, incubated with secondary antibodies (Abcam) in 5% non-fat milk for 1 h and washed again with PBS before being imaged on a Li-COR Odyssey imager. The primary antibodies used were rabbit anti-H2A (1:250, Cell Signaling Technology), rabbit anti-H2B (1:1,000, Abcam), rabbit anti-H3 (1:1,000, Abcam), mouse anti-H4 (1:1,000, Cell Signaling Technology), rabbit anti-NHP2 (1:1,000, Proteintech), rabbit anti-NOP10 (1:1,000, Abcam), rabbit anti-dyskerin (1:500, Santa Cruz Biotechnology) and rabbit anti-Strep (1:500, Genscript). All histone antibodies used were ChIP grade. The secondary antibodies used were goat anti-rabbit Alexa-Fluor 680 or 790 (1:5,000, Abcam) and goat anti-mouse Alexa-Fluor 680 (1:5,000, Abcam). Densitometry for quantification was performed in ImageJ.

### Human histone H2A–H2B purification

Human histone H2A–H2B dimer was purified as previously described, with modifications[50]. Bacterial-codon-optimized H2A and H2B with N-terminal His6-HRV-3C site fusions were individually expressed as inclusion bodies. HRV-3C is human rhinovirus 3C protease cleavage site. Two litres of transformed BL21 Star(DE3) cells was cultured at 37 °C in 2×TY medium supplemented with 50 µg ml$^{-1}$ kanamycin and 35 µg ml$^{-1}$ chloramphenicol to an optical density at 600 nm of 0.6, then induced with 1.0 mM IPTG followed by a 3 h incubation at 37 °C. Collected cells were resuspended in 50 ml wash buffer (50 mM Tris-HCl pH 8.0, 100 mM NaCl, 1 mM EDTA, 1 mM PMSF) supplemented with EDTA-free protease inhibitors (Roche) and frozen at −20 °C to lyse. Lysates were thawed, sonicated to reduce viscosity and centrifuged for 20 min at 4 °C and 25,000g. The pellet was washed by resuspension in wash buffer supplemented with 1% (v/v) Triton X-100, and spun for 10 min at 4 °C and 12,000 rpm. This was repeated twice more with wash buffer. The pellet was extracted in unfolding buffer (7.0 M urea, 50 mM Tris-HCl pH 8.0, 0.5 M NaCl, 30 mM imidazole, 0.1% Igepal CA-630, 1 mM DTT, 1 mM PMSF), centrifuged to remove insoluble material, then applied to a 5 ml HisTrap HP column (Cytiva) in buffer A (6.0 M urea, 50 mM Tris-HCl pH 8.0, 0.5 M NaCl, 30 mM imidazole, 1 mM DTT, 1 mM PMSF). The column was washed with 30 column volumes of buffer A and step-eluted to 100% buffer A supplemented with 500 mM imidazole. Histones H2A and H2B were mixed at equimolar ratios and adjusted to a concentration of 1 mg ml$^{-1}$ then refolded by extensive dialysis against refolding buffer (50 mM Tris-HCl pH 8.0, 2 M NaCl, 1 mM EDTA, 1 mM DTT). The final dialysis was performed overnight. The next day dialysate was concentrated using a 10,000 MWCO Amicon centrifugal concentrator (Millipore) and further purified using a Superdex 200 Increase 10/300 size exclusion column (Cytiva) in SEC buffer (50 mM Tris-HCl pH 8.0, 2 M NaCl, 1 mM EDTA, 1 mM DTT). Peak fractions were pooled, concentrated, checked for RNase contamination, aliquoted, flash-frozen in liquid nitrogen and stored at −80 °C before use.

### In vitro transcription and RNA purification

Transcription was performed using a linearized plasmid template of CR4/5. Each transcription reaction was composed of 4 mM of each of ATP, CTP, GTP and UTP, 50 mM Tris HCl pH 8.0, 1 mM spermidine, 10 mM DTT, 30 mM MgCl$_2$, 15 µg ml$^{-1}$ T7 polymerase and 100 µg ml$^{-1}$ linearized plasmid. The reaction mixture was incubated at 37 °C overnight and

spun at 5,000 rpm for 10 min to remove magnesium pyrophosphate precipitate. The supernatant was diluted with the same volume of water and precipitated with 6 volumes of ethanol at −20 °C overnight. The precipitated RNA was resuspended in formamide dye and run on an 8% denaturing acrylamide TBE gel with 7 M urea. The RNA band was excised from the gel using UV shadowing. For small-scale preparation, the RNA was extracted from the gel pieces by rotating them in crush and soak buffer (500 mM ammonium acetate, 1 mM EDTA, 0.5% SDS) overnight at 37 °C. The gel pieces were removed by filtration. The RNA was phenol:chloroform-extracted twice then precipitated overnight at −20 °C in 2.5 volumes of ethanol. The RNA pellet was resuspended in TE, aliquoted and stored at −80 °C until use.

## Electrophoretic mobility shift assays

5′ $^{32}$P-radiolabelled CR4/5 domain was refolded by heating to 95 °C for 5 min in TE supplemented with 2 mM MgCl$_2$, then allowed to cool to room temperature overnight. Increasing concentrations of histone H2A–H2B dimer (0.25–20 pmol) were incubated with 1 fmol radiolabelled CR4/5 on ice in a total volume of 10 µl EMSA buffer (50 mM Tris-HCl pH 8.0, 250 mM NaCl, 1 mM MgCl$_2$, 100 µg ml$^{-1}$ BSA, 25 µg ml$^{-1}$ T11 RNA[51], 0.5 mM DTT). After 1 h, Ficoll was added to a final concentration of 2.5% and each sample was resolved by electrophoresis on a 5% native 37.5:1 polyacrylamide gel at 4 °C in 0.5× TBE, dried and visualized with phosphorimaging. Bands were quantified with ImageQuant (Cytiva) and analysed with Prism 8 using a single-site saturation binding model (GraphPad)[52].

## Cryo-EM electron microscopy

For cryo-EM data collection, we applied 3 µl of purified human telomerase on a C-flat-T-50 4/2 grids (Protochips), which were precoated with a layer of approximately 5–6-nm-thick homemade continuous carbon film and glow-discharged using a Sputter coater discharger (model Edwards S150B). The grids were blotted for 5 s at 100% humidity and 4 °C and vitrified in liquid ethane using an FEI Vitrobot MK IV. Data collection was performed on an in-house ThermoFisher Titan Krios transmission electron microscope operated at 300 kV and equipped with a Gatan K3 direct electron detector camera and a GIF Quantum energy filter. Images were collected automatically using the Serial-EM package[53] in counting mode with a physical pixel size of 1.11 Å per pixel, with a total electron dose of 47 electrons per Å$^2$ during a total exposure time of 2.49 s, dose-fractionated into 48 movie frames (Extended Data Table 1). We used a slit width of 20 eV on the energy filter and a defocus range of 1.2–3.5 µm. A total of 43,693 micrographs were collected from two separate sessions.

## Image processing

Most steps of data processing were done in RELION 3.1[54], unless otherwise stated (Extended Data Figs. 1, 5a). The movies for each micrograph were first corrected for drift and dose-weighted using RELION. Contrast-transfer function (CTF) parameters were estimated for the drift-corrected micrographs using CTFFIND4 within RELION[55]. The two datasets were first processed separately and combined at a later stage.

For the first dataset, we rescaled the good 2D class averages from the previous dataset collected with a K2 camera[3] and used them as references for auto-picking. These particles were binned by 4 and extracted with a box size of 100$^2$ pixels for 3D classification. Particles from the best 3D class were unbinned and subjected to a round of 2D classification. The best 2D class averages from this 2D classification were then used for the second round of auto-picking. A total of 8,401,685 particles were picked, binned by 4 and extracted with a box size of 100$^2$ pixels. We performed 3D classification of these particles with 8 sub-classes, angular sampling of 15°, regularization parameter $T$ of 4 and an initial model from the previous published dataset. We selected 3D classes with an intact H/ACA lobe and catalytic core, and ran reference-free 2D classification to remove any remaining bad particles and contaminants.

The resulting 1,853,803 particles with two intact lobes were unbinned and refined to yield an 8.1 Å reconstruction. As expected, this reconstruction does not show secondary structural features expected at this resolution owing to the conformational heterogeneity between the two lobes. We divided the structure into the H/ACA lobe and the catalytic core, and performed signal subtraction with recentering to obtain particle images containing and centred at only the lobe of interest. We also downsized the box size of the H/ACA lobe and the catalytic core to 240$^2$ pixels and 180$^2$ pixels, respectively, during this process to speed up downstream processing. For each lobe, 3 rounds of 3D classification into 6 classes were run for 25 iterations in each round, with angular samplings of 15°, 7.5° and 3.75°, respectively. The best class for the H/ACA lobe (consisting of 591,197 particles) was refined to 3.9 Å resolution. These signal-subtracted particles were subsequently reverted to the original particles for Bayesian polishing. The polished particles were refined and signal subtraction with recentering was performed again to remove the density from the catalytic core. We refined the signal-subtracted polished particles to 3.9 Å resolution and used the angular assignments from this refinement for alignment-free 3D classification. A subset of 98,663 particles from the best 3D class was selected, and refined to 3.7 Å resolution. For the catalytic core, a subset of 888,369 particles from the best two classes were selected and refined to 4.1 Å resolution. They were reverted to the original particles for Bayesian polishing. The refined polished particles were subjected to signal subtraction with recentering to remove the density from the H/ACA lobe. They were then refined to 4.3 Å resolution. Another round of alignment-free 3D classification was performed to resolve further heterogeneity. A subset of 133,816 particles from the best class was selected and refined to 4.1 Å resolution. The best subsets for each lobe were later combined with the best subsets of particles from the second dataset.

For the second dataset, 2D references from the first dataset were used for auto-picking, resulting in 7,358,749 picked particles. We used a similar strategy as for the first dataset with 3D classification followed by 2D classification to yield 1,865,927 particles, which were unbinned and refined to 6.7 Å resolution. We performed signal subtraction and applied similar classification and refinement strategies to those used for the first dataset for the individual lobes. For the catalytic core, we obtained a subset of 34,722 particles, which were refined to 4.2 Å resolution. For the H/ACA lobe, we also applied similar strategies, except Bayesian polishing did not improve the reconstruction. A best subset of 106,002 particles was refined to 3.6 Å resolution.

We combined the best subsets of particles from the two datasets for each lobe. The combined subset of 168,538 particles for the catalytic core was refined to 3.9 Å resolution. Beam-tilt and defocus refinement further improved the reconstruction to 3.8 Å resolution[56]. The 204,665 particles for the H/ACA lobe were refined to 3.6 Å resolution, which was improved to 3.4 Å resolution with beam-tilt and defocus refinement.

To obtain the reconstruction of the whole complex containing both lobes, we combined the 1,853,803 particles from the first dataset and the 1,865,927 particles from the second dataset before signal subtraction and performed 3D classification at bin 4 (Extended Data Fig. 1). The best two subsets were unbinned and refined. The first subset of 484,847 particles (3D class 2) was refined to 4.5 Å resolution. However, this reconstruction exhibited preferential orientation in the H/ACA lobe. The second subset of 463,013 particles (3D class 5) was refined to 6.6 Å resolution. For both subsets, the H/ACA lobe was better aligned than the catalytic core, and the resulting maps were heterogeneous in resolution, indicative of a high degree of conformational heterogeneity (Extended Data Fig. 2e, f).

To analyse the conformational dynamics within each of these two subsets, we performed multibody refinement on each of the subsets using two masks for the H/ACA lobe and the catalytic core (Extended Data Fig. 5a–c). This was followed by principal component analysis using six eigenvectors to identify the motions between the two lobes[13].

# Article

The first subset was refined to 3.9 Å and 10.3 Å resolution for the H/ACA lobe and the catalytic core, respectively. The second subset was refined to 4.3 Å and 9.3 Å resolution for the H/ACA lobe and the catalytic core, respectively. The two extreme states in each volume series for the first six principal components (Extended Data Fig. 5b, c) clearly illustrated the conformational flexibility between the two lobes.

All refinements were performed using fully independent data half-sets and resolutions are reported based on the Fourier shell correlation (FSC) = 0.143 criterion[57,58] (Extended Data Fig. 2a). FSCs were calculated with a soft mask. Maps were corrected for the modulation transfer function of the detector and sharpened by applying a negative $B$-factor as determined either by the post-processing function of RELION or by a user-defined value. Local resolution was calculated within RELION (Extended Data Fig. 2c–f).

## Histone H2B identification by molecular replacement

To identify the previously unassigned density, we located the centre of mass of the density using COOT and used a map within a 30 Å radius from this centre of mass for molecular replacement search against the BALBES database using MolRep[26,59,60]. The search returned histone H2B (PDB 1KX5, chain D[27]) as the top hit with a contrast score of 3.90 with excellent fit. Other top hits with contrast scores above 3 showed poor fits. The histone H2A–H2B dimer extracted from the nucleosome structure (chains C and D, PDB 1KX5) showed perfect fit in our unassigned density.

## Model building and refinement

All model building was performed de novo in COOT[61] using the placement of the homology models of the 8 Å structure[3] in the 3.4 Å and 3.8 Å maps of the H/ACA lobe and the catalytic core, respectively. To aid modelling building, we converted the maps to MTZ format using REFMAC5.8, which can be blurred and sharpened in COOT[59]. We first built the RNA manually. For hTR in the catalytic core, we used DRRAFTER to model regions that were more ambiguous, as described in more detail below[14]. The top 10 scoring models from DRRAFTER were manually inspected for fitting in the maps. The best-fit models for each region were incorporated into the manually built RNA coordinates. We further improved RNA geometry for hTR in both lobes using ERRASER[62]. The resulting models were fixed manually to remove clashes with the protein models before model refinement. Extended Data Table 2 summarizes the modelled components. The models were refined first in real-space using Phenix[63] and then in reciprocal space using REFMAC5.8[64] with protein secondary structure restraints calculated using PROSMART[65] and RNA base-pair and stacking restraints using LIBG[59]. The FSC model versus map was calculated using Phenix[63] (Extended Data Fig. 2b). The geometries of the refined models were analysed by MolProbity[66]. A summary of deposited maps, models and refinement statistics are provided in Extended Data Table 1. As an additional validation of the RNA register assignment, we shifted the registers of important RNA regions including the template, CAB box, H and ACA boxes in the refined models by one residue and calculated model-to-map cross-correlations for these alternative models using Phenix[63]. As expected, these models show poorer cross correlations as compared to our final refined models (Supplementary Table 1).

## DRRAFTER modelling of hTR

For the hTR region in the catalytic core, the density map allowed for manual tracing of positions 32–36, 46–56, 64–67, 79–83, 89–131, 142–150, 163–192, 242–246, 256–273, 282–317 and 322–327. DRRAFTER[14] was used to model the remaining nucleotides (18–31, 37–45, 57–63, 68–78, 84–89, 132–142, 195–208, 234–241, 247–255, 274–281, 318–324 and 328–337). Protein density was subtracted from the map by removing a 3 Å zone around protein residues with Chimera, and the map was low-pass-filtered to 4 Å with EMAN2[67]. Manually built RNA residues and all protein coordinates in the catalytic core were included as a

single rigid body during modelling. Additionally, A-form helices for P1a (18–31 and 195–208), P2a.1 (68–72 and 136–140), and P4 (234–240 and 331–337) were included as rigid bodies. The 10 top-scoring models have a convergence (mean pairwise root mean square deviation (r.m.s.d.)) of 4.54 Å, yielding an estimated r.m.s.d. accuracy of 4.57 Å for residues modelled with DRRAFTER. These ensembles are included in Supplementary Data 1.

For the full-length maps, hTR residues that were built using the high-resolution density for each lobe separately above were fit as rigid bodies into the lower-resolution full-length classes 2 and 5 dual-lobe maps (Extended Data Figs. 1, 2, 5a) using Chimera and COOT. For the catalytic core, all protein residues and hTR residues 38–150, 163–186, 256–261 and 295–315 were fit, and for the H/ACA domain, all protein residues and hTR residues 211–218, 362–392 and 397–449 were fit. Coordinates for helix P6b were not included at this stage, as the fitted position did not match the density for this helix in the dual-lobe maps. A 5 Å zone of density around the fitted coordinates was subtracted with Chimera, and the resulting map was segmented using the Segment Map tool of Chimera; segments were selected to preserve density for only helix P6b and the hTR linker. DRRAFTER was used to model helix P6b and the hTR linker (residues 18–37, 187–210, 219–255 and 316–362). Fitted catalytic core and H/ACA domain coordinates were included as a rigid body during modelling. Additionally, A-form helices were included as rigid bodies for P1a (18–31 and 195–208), P4.1 (225–231, 341–344 and 346–348), P4.2 (234–240 and 331–337), P5 (243–247 and 322–326) and P6b (268–275, 280–284 and 286–288). For models built into class 2, the 10 top-scoring models have a convergence of 8.63 Å for helix P6b and the hTR linker stems (P4.2 and P1) (Fig. 1d), yielding an estimated r.m.s.d. accuracy of 8.54 Å for these regions (Extended Data Fig. 5d, Supplementary Data 2). For models built into class 5, the 10 top-scoring models have a convergence of 10.58 Å for helix P6b and the hTR linker stems (P4.2 and P1) (Fig. 1d), yielding an estimated r.m.s.d. accuracy of 10.43 Å for these regions (Extended Data Fig. 5e, Supplementary Data 3).

## Map and model visualization

The signal subtracted maps for the catalytic core and the H/ACA lobe were recentred at the centre of each individual map. Therefore, for illustrations in Fig. 1, we fitted them to the full 3D class 2 map (Extended Data Fig. 5). Maps were visualized in Chimera and ChimeraX[68,69] and all model illustrations were prepared using either Pymol (www.pymol.org) or Chimera/ChimeraX.

## Reporting summary

Further information on research design is available in the Nature Research Reporting Summary linked to this paper.

## Data availability

Raw gels are provided in Supplementary Fig. 1. Replicates of the activity assays and immunoblotting experiments shown in Fig. 3d, e and quantification are included in Supplementary Fig. 2. Full mass spectrometry data and coordinates of hTR from DRRAFTER modelling are provided in the Supplementary Information. Cryo-EM maps of the catalytic core, H/ACA lobes and the whole telomerase maps (class 2 and class 5) with both lobes have been deposited with the Electron Microscopy Data Bank under accession numbers EMD-12174, EMD-12177, EMD-12175 and EMD-12176. Refined atomic coordinates for the catalytic core and H/ACA lobes are deposited with the PDB under accession numbers 7BG9 and 7BGB. The rigid body fitted models of the catalytic core and the H/ACA lobes into the whole telomerase maps (class 2 and class 5) are included as a Pymol session in Supplementary Data 2, 3. The BALBES database was provided internally by the BALBES developers, and is available upon request to the corresponding author. Source data are provided with this paper.

49. Wu, R. A., Dagdas, Y. S., Yilmaz, S. T., Yildiz, A. & Collins, K. Single-molecule imaging of telomerase reverse transcriptase in human telomerase holoenzyme and minimal RNP complexes. *eLife* **4**, e08363 (2015).
50. Luger, K., Rechsteiner, T. J. & Richmond, T. J. in *Methods in Enzymology* Vol. 304 (eds. Wassarman P. M. & Wolffe, A. P.) 3–19 (Elsevier, 1999).
51. Nguyen, T. H. D. *Structural and Biochemical Studies of Spliceosomal Activation*. PhD thesis, Univ. of Cambridge (2014).
52. Goodrich, J. A. & Kugel, J. F. *Binding and Kinetics for Molecular Biologists* (Cold Spring Harbor Laboratory, 2007).
53. Mastronarde, D. N. Automated electron microscope tomography using robust prediction of specimen movements. *J. Struct. Biol.* **152**, 36–51 (2005).
54. Zivanov, J. et al. New tools for automated high-resolution cryo-EM structure determination in RELION-3. *eLife* **7**, e42166 (2018).
55. Rohou, A. & Grigorieff, N. CTFFIND4: fast and accurate defocus estimation from electron micrographs. *J. Struct. Biol.* **192**, 216–221 (2015).
56. Zivanov, J., Nakane, T. & Scheres, S. H. W. Estimation of high-order aberrations and anisotropic magnification from cryo-EM data sets in *RELION*-3.1. *IUCrJ* **7**, 253–267 (2020).
57. Rosenthal, P. B. & Henderson, R. Optimal determination of particle orientation, absolute hand, and contrast loss in single-particle electron cryomicroscopy. *J. Mol. Biol.* **333**, 721–745 (2003).
58. Chen, S. et al. High-resolution noise substitution to measure overfitting and validate resolution in 3D structure determination by single particle electron cryomicroscopy. *Ultramicroscopy* **135**, 24–35 (2013).
59. Brown, A. et al. Tools for macromolecular model building and refinement into electron cryo-microscopy reconstructions. *Acta Crystallogr. D* **71**, 136–153 (2015).
60. Vagin, A. & Teplyakov, A. Molecular replacement with MOLREP. *Acta Crystallogr. D* **66**, 22–25 (2010).
61. Casañal, A., Lohkamp, B. & Emsley, P. Current developments in *Coot* for macromolecular model building of electron cryo-microscopy and crystallographic data. *Protein Sci.* **29**, 1055–1064 (2020).
62. Chou, F.-C., Echols, N., Terwilliger, T. C. & Das, R. RNA structure refinement using the ERRASER–Phenix pipeline. *Methods Mol. Biol.* **1320**, 269–282 (2016).
63. Afonine, P. V. et al. Towards automated crystallographic structure refinement with phenix. refine. *Acta Crystallogr. D* **68**, 352–367 (2012).
64. Murshudov, G. N. et al. REFMAC5 for the refinement of macromolecular crystal structures. *Acta Crystallogr. D* **67**, 355–367 (2011).
65. Nicholls, R. A., Fischer, M., McNicholas, S. & Murshudov, G. N. Conformation-independent structural comparison of macromolecules with ProSMART. *Acta Crystallogr. D* **70**, 2487–2499 (2014).
66. Williams, C. J. et al. MolProbity: more and better reference data for improved all-atom structure validation. *Protein Sci.* **27**, 293–315 (2018).
67. Tang, G. et al. EMAN2: an extensible image processing suite for electron microscopy. *J. Struct. Biol.* **157**, 38–46 (2007).
68. Goddard, T. D. et al. UCSF ChimeraX: meeting modern challenges in visualization and analysis. *Protein Sci.* **27**, 14–25 (2018).
69. Pettersen, E. F. et al. UCSF Chimera—a visualization system for exploratory research and analysis. *J. Comput. Chem.* **25**, 1605–1612 (2004).
70. Podlevsky, J. D., Bley, C. J., Omana, R. V., Qi, X. & Chen, J. J. The telomerase database. *Nucleic Acids Res.* **36**, D339–D343 (2008).
71. Tesmer, V. M., Smith, E. M., Danciu, O., Padmanaban, S. & Nandakumar, J. Combining conservation and species-specific differences to determine how human telomerase binds telomeres. *Proc. Natl Acad. Sci. USA* **116**, 26505–26515 (2019).

# Article



**Extended Data Fig. 1 | Image processing scheme.** Summary of the data processing strategies that yielded the reconstructions described in this Article.
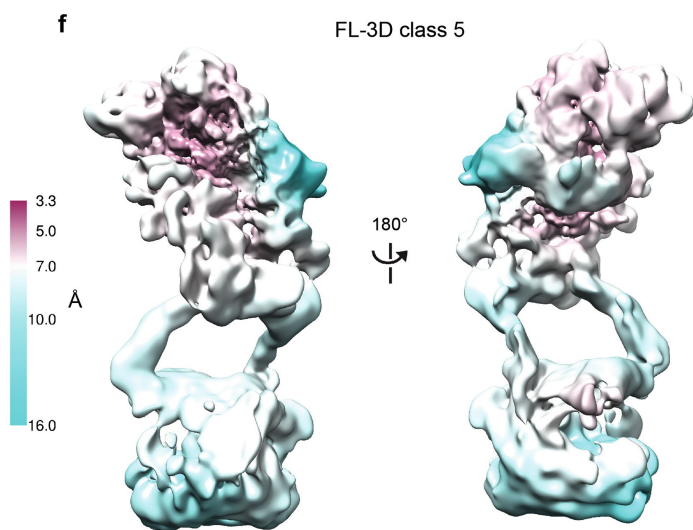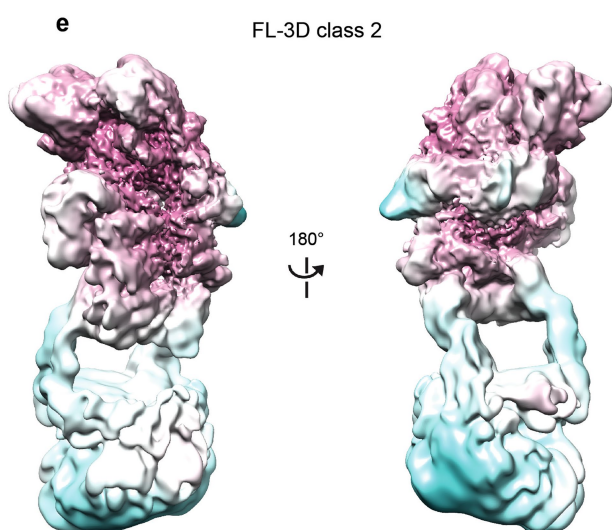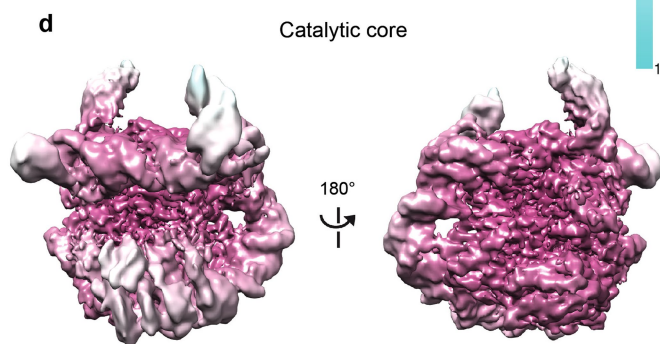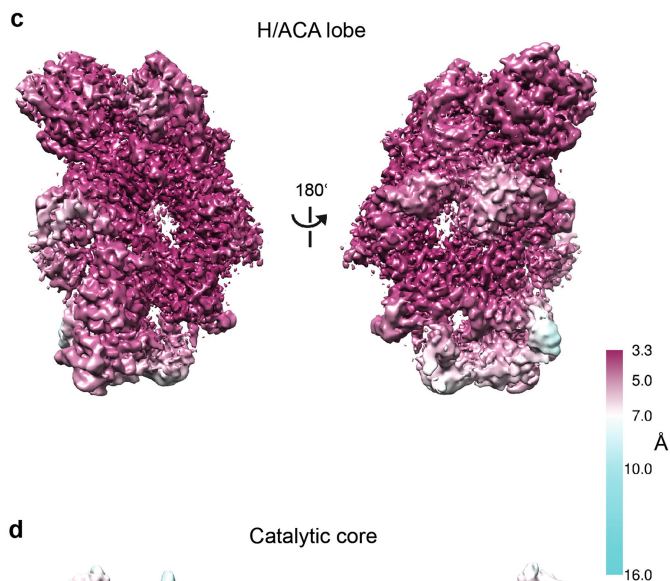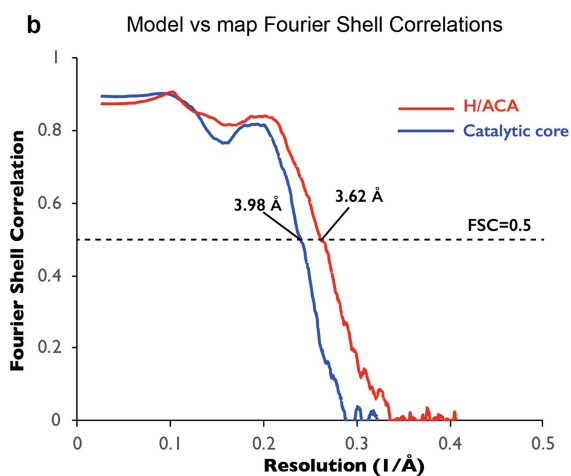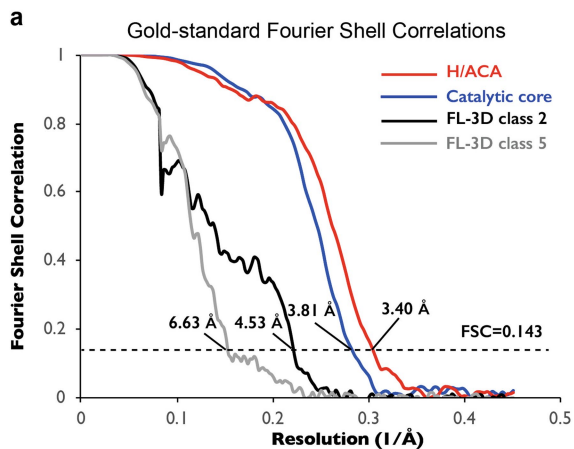
**Extended Data Fig. 2 | Local resolution and resolution estimation.**
**a**, Gold-standard FSC curves for maps of H/ACA lobe, the catalytic core and the best two full-length classes. Resolutions were estimated at FSC = 0.143. **b**, FSC curves for the refined H/ACA and catalytic core models versus the corresponding maps. Resolutions were estimated at FSC = 0.5. **c–f**, Local resolution estimated by RELION 3.1[54] for the H/ACA lobe (**c**), the catalytic core (**d**), full-length 3D class 2 (**e**) and full-length 3D class 5 (**f**). For direct comparisons, the same local resolution range (3.3–16 Å) was used for all maps.
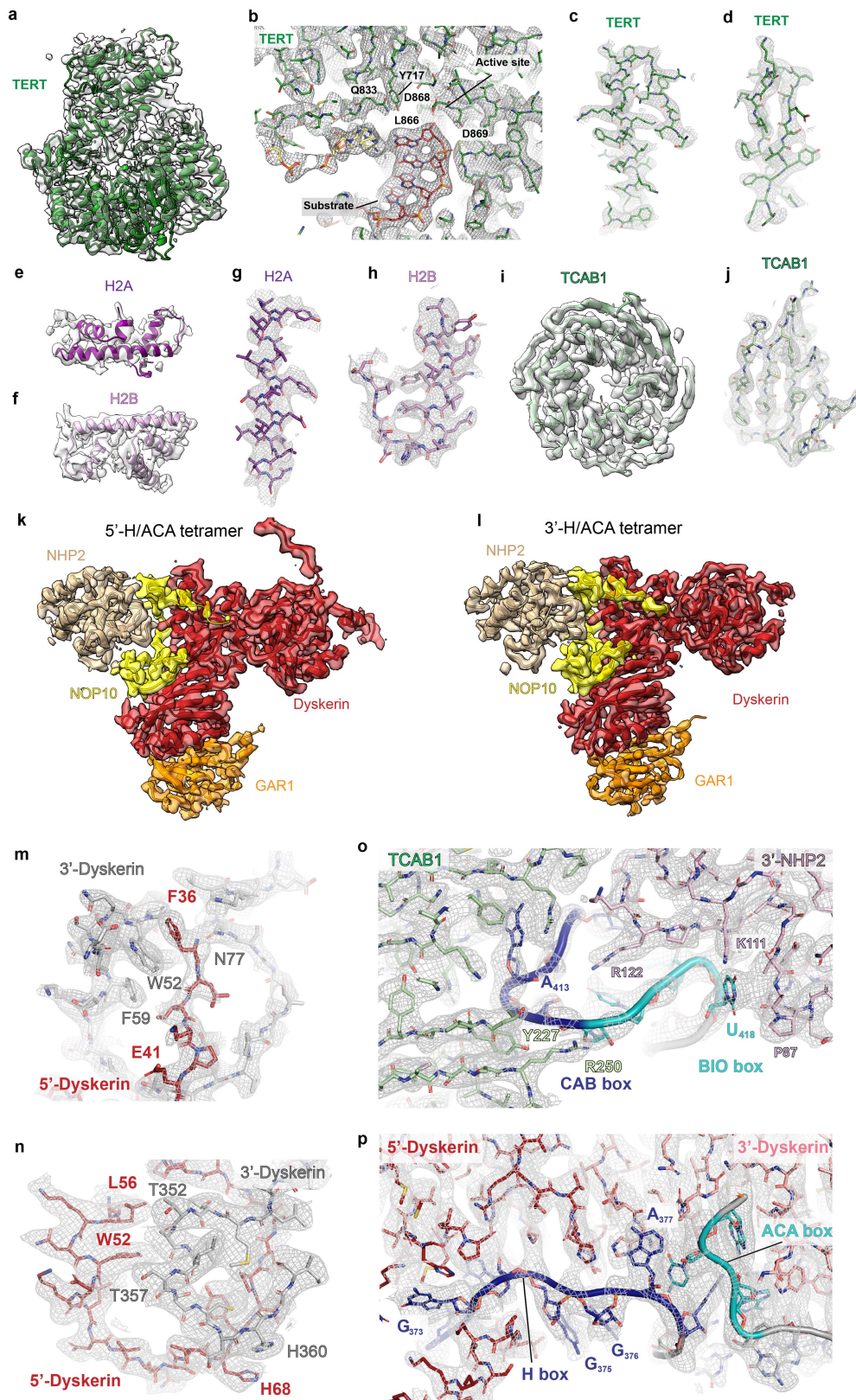
**Extended Data Fig. 3 | Electron microscopy density of protein components.**
**a**, **e**, **f**, **i**, **k**, **l**, Full densities of TERT (**a**), histone H2A (**e**), histone H2B (**f**), TCAB1 (**i**),
5′ H/ACA tetramer (**k**) and 3′ H/ACA tetramer (**l**). **b**, Close-up view of the active
site density of TERT with an empty nucleotide-binding pocket (Extended
Data Fig. 6f). **c**, **d**, Representative electron microscopy densities of TERT.
**g**, **h**, **j**, Representative electron microscopy densities of histone H2A (**g**),
histone H2B (**h**) and TCAB1 (**j**). **m**, Close-up view of the density of the N-terminal
extension of the 5′ dyskerin bound to a hydrophobic pocket within the

3′ dyskerin (Fig. 4c). **n**, Close-up view of the density of helix 352–375 of the
3′ dyskerin bound to the equivalent hydrophobic pocket as in **m** within the
5′ dyskerin (Fig. 4d). **o**, Close-up view of the density of the P8 stem loop of hTR,
which contains the CAB and BIO boxes that interact with TCAB1 and the 3′ NHP2
(Extended Data Figs. 4l, 8d). **p**, Close-up view of the density of the H and
ACA boxes interacting with the two dyskerin molecules (Extended Data
Figs. 4k, 8c).
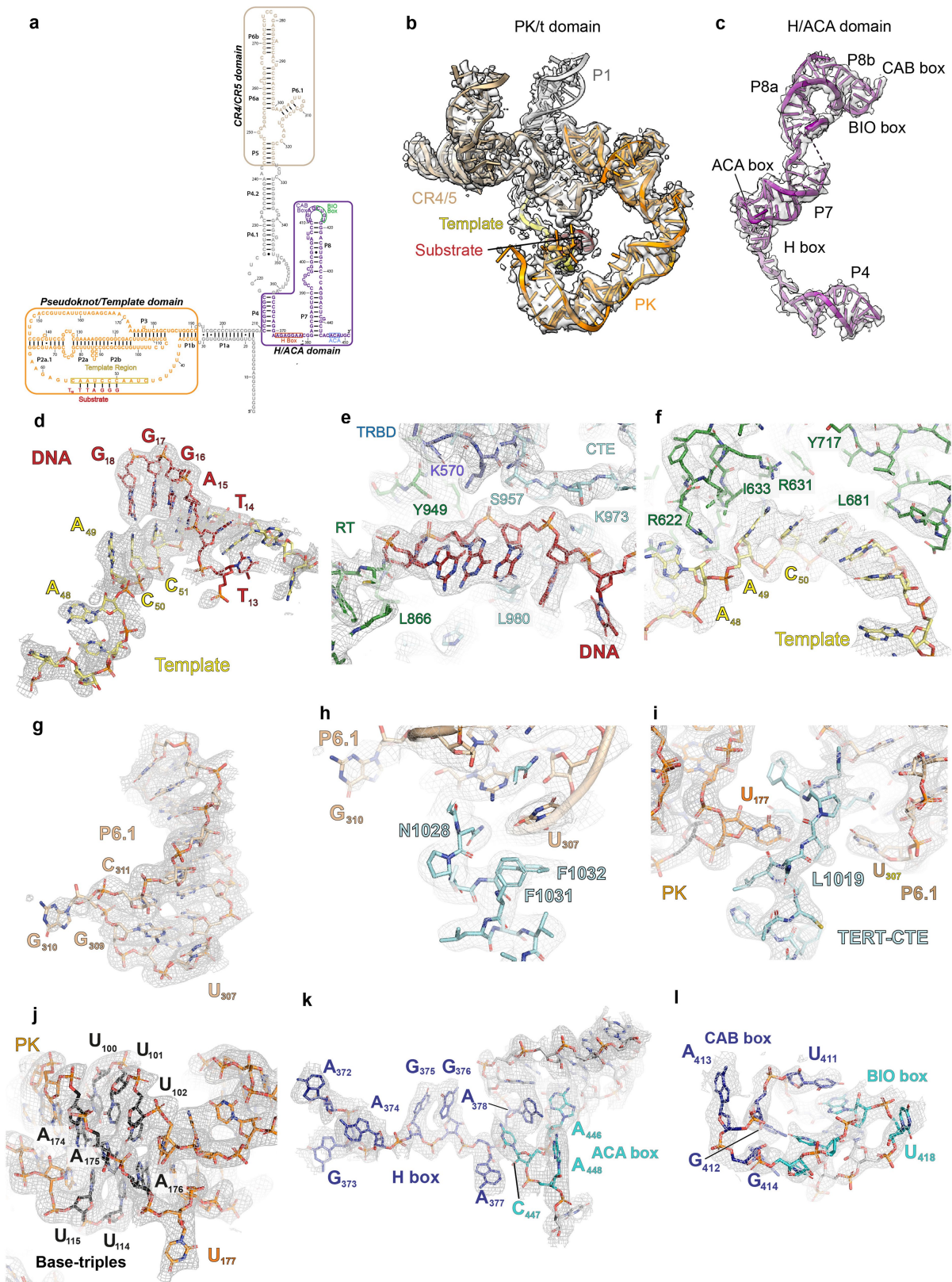
**Extended Data Fig. 4** | See next page for caption.

# Article

**Extended Data Fig. 4 | Electron microscopy density of hTR and DNA substrate. a**, Secondary structure schematic of hTR based on the structure. This figure was modified from the telomerase database[70]. **b, c**, Full density of hTR in the catalytic core (**b**) and the H/ACA lobe (**c**). **d**, Close-up view of the density of interactions between the DNA substrate and hTR template (Fig. 2b). **e**, Close-up view of density of the DNA substrate and neighbouring residues of TERT (Extended Data Fig. 6d). **f**, Close-up view of density of the RNA template region and neighbouring residues of TERT (Extended Data Fig. 6e). **g**, Density of the P6.1 hairpin of the CR4/5 domain. Labelled residues are highlighted in Fig. 3a. **h**, Close-up review of the density of the P6.1 stem loop interacting with residues of the CTE domain of TERT (**g**, Fig. 3a). **i**, Close-up view of the density of residue L1019 of TERT, which interacts with the two flipped-out nucleotides, U177 of the PK and U307 of the P6.1 stem loop as highlighted in Fig. 3b. **j**, Representative density of the PK containing the base triples, which are highlighted in black. Nucleotide U113 is modelled but not visible in this view. **k**, Density of the H and ACA boxes (Extended Data Fig. 3p). **l**, Density of the P8 stem loop (Extended Data Fig. 3o).

**a**      Datasets 1 and 2, Global classification

**3D class 2**
484,847 particles
3D refinement
Mask creation

**3D class 5**
463,013 particles
3D refinement
Mask creation

H/ACA lobe

Catalytic core

Multibody refinement
Principal component analysis

Multibody refinement
Principal component analysis

**b**    **3D class 2**

Component 1    Component 2    Component 3    Component 4    Component 5    Component 6

H/ACA lobe   Catalytic core

**c**    **3D class 5**

Component 1    Component 2    Component 3    Component 4    Component 5    Component 6

H/ACA lobe   Catalytic core

**d**    **FL-3D class 2**
Top 10 hTR ensembles from DRRAFTER

180°

hTR       hTR

**e**    **FL-3D class 5**
Top 10 hTR ensembles from DRRAFTER

180°

hTR       hTR

**Extended Data Fig. 5 | Multibody refinement and conformational dynamics analysis of the full-length structure. a**, Summary of the multibody refinement strategy and principal component analysis[13]. The best two subsets from global 3D classification were subjected to multibody refinement using two masks for the H/ACA lobe (yellow) and the catalytic core (cyan). **b**, Principal component analysis for 3D class 2. **c**, Principal component analysis for 3D class 5. The first and last frames of the eigenvector series of the first six principal components are shown. Curved arrows indicate the movements. **d**, Top 10 hTR ensembles modelled by DRRAFTER into the refined full-length 3D class 2 map (Supplementary Data 2). **e**, Top 10 hTR ensembles modelled by DRRAFTER into the refined full-length 3D class 5 map (Supplementary Data 3). hTR is shown in blue, and the protein subunits are in grey.

# Article
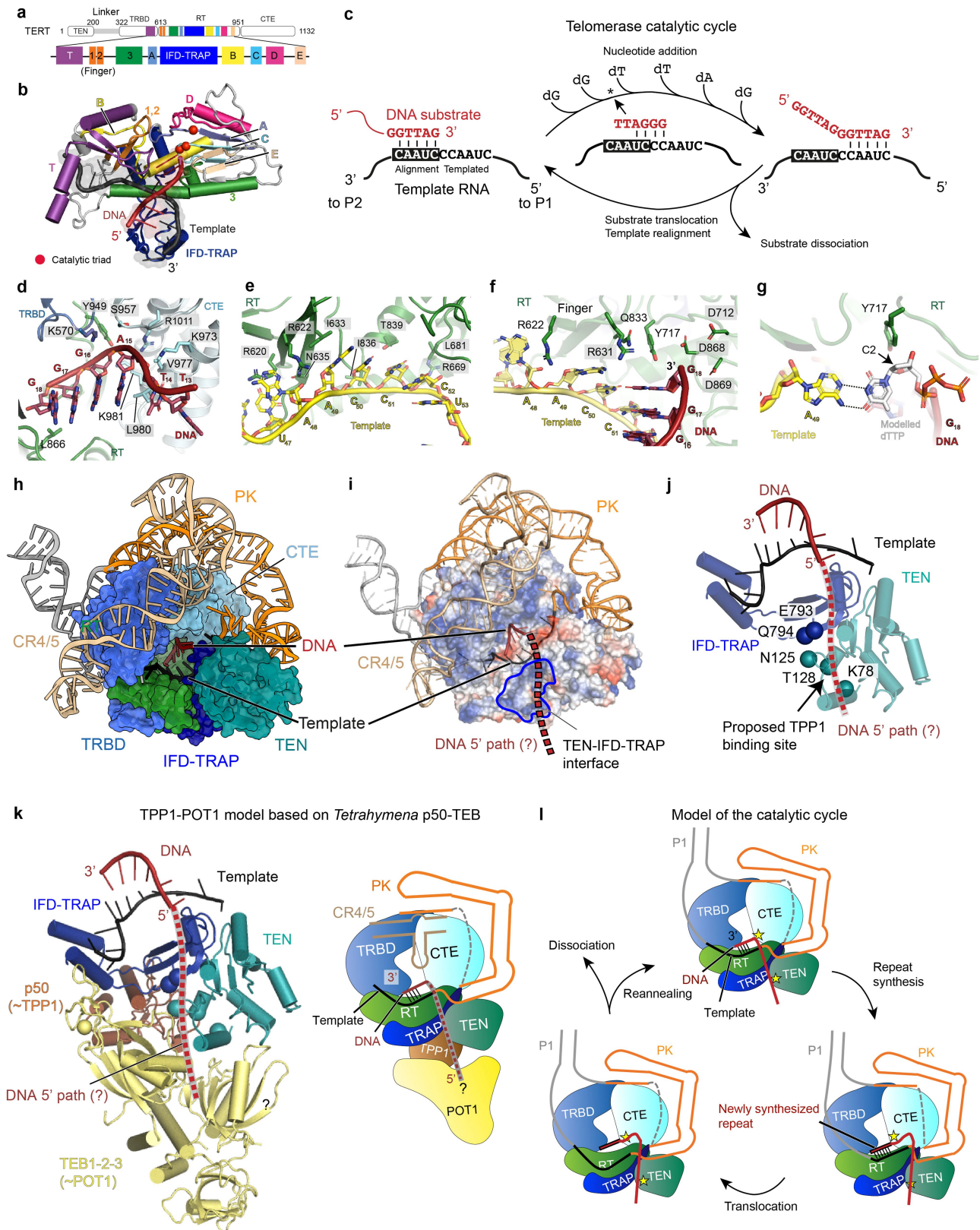


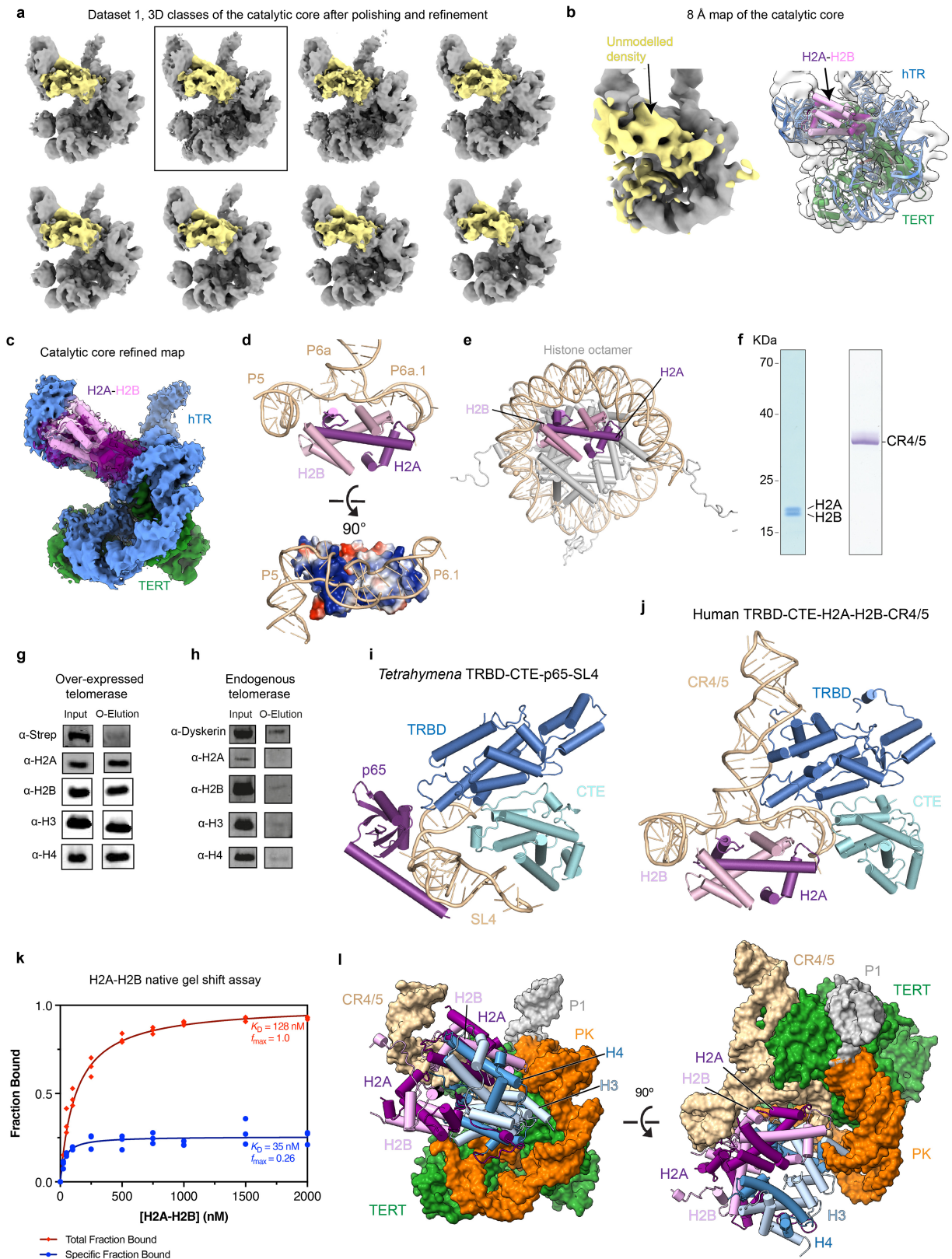**Extended Data Fig. 6** | See next page for caption.

**Extended Data Fig. 6 | Telomerase catalytic cycle and DNA path. a**, Domain architecture of human TERT and conserved motifs that are often observed in reverse transcriptases[70]. **b**, TERT conserved motifs shown in **a**, and their interactions with the template and DNA substrate. **c**, A model for the telomerase catalytic cycle. The template region of hTR is divided into an alignment region and a template region. The telomeric DNA repeat first binds to the alignment region, followed by six consecutive nucleotide additions using the template region. After the synthesis of the full telomeric repeat, the DNA substrate translocates to bind the alignment region to start another round of repeat synthesis. The state captured in our structure is indicated with an asterisk. **d**, Interactions between the 3′ telomeric TTAGGG repeat of the substrate and TERT. **e**, Interactions between the template region of hTR and TERT. **f**, TERT active site in a prenucleotide state. D712, D868 and D869 form the catalytic triad for nucleotide addition (Extended Data Fig. 3b). **g**, Modelled dTTP (PDB 1T3N[22]) in the vacant nucleotide site of TERT. The C2 ribose is indicated. **h**, Structure of human TERT with PK/t and CR4/5 domains of hTR and DNA. **i**, Electrostatic surface potential of human TERT with hTR and the DNA substrate shown in the same view as in **h**. The highlighted human TEN–IFD–TRAP interface (in blue) is positively charged and could potentially bind the 5′ end of the DNA substrate in human telomerase. **j**, IFD–TRAP and TEN domains of TERT. Residues that are known to affect TPP1 binding to TERT are highlighted as spheres[71]. The proposed DNA path would bring it close to the proposed TPP1-binding site on the TEN domain. **k**, Model of TPP1–POT1 bound to human TEN domain, based on the *Tetrahymena* p50–TEB complex. Despite the similar overall domain arrangements, the domains of *Tetrahymena* and human TERT do not align well as a whole. To obtain the model, we superposed the *Tetrahymena* TEN domain–p50–TEB1–TEB2–TEB3 complex (PDB 6D6V[16]) onto the human TEN domain. **l**, Model of telomerase catalytic cycle. Telomerase template RNA binds the telomeric DNA substrate by base-pairing. The DNA-binding sites on TERT are indicated by yellow stars. One binding site is provided by motif T and the CTE domain of TERT near the active site, as observed in the structure (Fig. 2d and **d**). The second binding site is proposed to be provided by the TEN domain at the 5′ end of the DNA. After the synthesis of a full telomeric repeat, the nascent DNA undergoes translocation and rebinding to the template RNA. We propose that the two DNA-binding sites form an anchor site to allow DNA retention for multiple rounds of repeat synthesis.

**a** Dataset 1, 3D classes of the catalytic core after polishing and refinement

**b** 8 Å map of the catalytic core

Unmodelled density

H2A-H2B
hTR
TERT

**c** Catalytic core refined map

H2A-H2B
hTR
TERT

**d**
P6a
P5
P6a.1
H2B
H2A
90°
P5
P6.1

**e** Histone octamer
H2B
H2A

**f** KDa
70
40
25
15
H2A
H2B
CR4/5

**g** Over-expressed telomerase
Input  O-Elution
α-Strep
α-H2A
α-H2B
α-H3
α-H4

**h** Endogenous telomerase
Input  O-Elution
α-Dyskerin
α-H2A
α-H2B
α-H3
α-H4

**i** *Tetrahymena* TRBD-CTE-p65-SL4
TRBD
p65
CTE
SL4

**j** Human TRBD-CTE-H2A-H2B-CR4/5
CR4/5
TRBD
CTE
H2B
H2A

**k** H2A-H2B native gel shift assay

$K_D = 128$ nM
$f_{max} = 1.0$

$K_D = 35$ nM
$f_{max} = 0.26$

Fraction Bound — [H2A-H2B] (nM)

— Total Fraction Bound
— Specific Fraction Bound

**l**
CR4/5
H2B
H2A
P1
H4
H3
PK
H2A
H2B
H2B
TERT
90°
CR4/5
P1
TERT
H2A
H2B
PK
H2A
H2B
H3
H4

**Extended Data Fig. 7** | See next page for caption.

**Extended Data Fig. 7 | Identification of histone H2A and H2B as subunits of the human telomerase holoenzyme. a**, Three-dimensional classification of the catalytic core (dataset 1), showing the presence of the unaccounted-for density (in yellow). The best class (boxed) has the most homogenous density, and was selected for the final refinement. Similar observations were made with the second dataset. **b**, The 8 Å catalytic core map (in grey) with the previously unmodelled density (in yellow)[3] (left) and with the model of the catalytic core obtained from this work fitted into it (right). The density assigned as the histone H2A–H2B dimer coincided with the unmodelled density from the previous work. **c**, The refined catalytic core map, with hTR, TERT and histone H2A–H2B segmented in different colours. **d**, Top, interactions between CR4/5 and the histone H2A–H2B dimer in human telomerase. Bottom, electrostatic surface potential of the histone dimer and the positively charged surface used for interacting with the CR4/5. **e**, Nucleosome structure. The histone H2A–H2B dimer is coloured and oriented the same way as in **d**. This shows that the histone H2A–H2B dimer uses the same surface to bind both nucleosomal DNA and CR4/5 (PDB 1KX5[27]). **f**, Purified histone H2A–H2B and CR4/5 RNA used for electrophoretic mobility shift assay in Fig. 3f. No RNA ladders were loaded with the CR4/5 RNA. **g**, Immunoblots of crude lysate of HEK 293T cells transfected with twin Strep-TERT and hTR expression constructs (input) and oligonucleotide elution from 2′-*O*-methyl purification (Fig. 3c). These samples were immunoblotted for Strep and histones H2A, H2B, H3 and H4. The presence of histones H2A, H2B, H3 and H4 was also confirmed by mass spectrometry (Supplementary Data 4). **h**, Immunoblots of crude lysate of HEK 293T cells (input) and oligonucleotide elution from 2′-*O*-methyl purification. These samples were immunoblotted for dyskerin, and histones H2A, H2B, H3 and H4. **i**, Structure of the *Tetrahymena* TRBD–CTE–p65 and stem loop 4 (SL4) (PDB 6D6V[16]). **j**, Structure of human TRBD–CTE–H2A–H2B and CR4/5. **k**, Quantification of the electrophoretic mobility shift assays shown in Fig. 3f for $K_d$ determination. 'Total fraction bound' reflects the quantification of free probe depletion against total probe with increasing histone concentration. 'Specific fraction bound' reflects the quantification of the increasing discrete shifted complex band against total probe with increasing histone concentration. Points represent values from three independent replicates (Supplementary Fig. 1). **l**, Superposition of the histone octamer structure, with flexible histone tails removed, onto the histone H2A–H2B dimer bound to the human telomerase catalytic core in two different views (PDB 1KX5[27]).
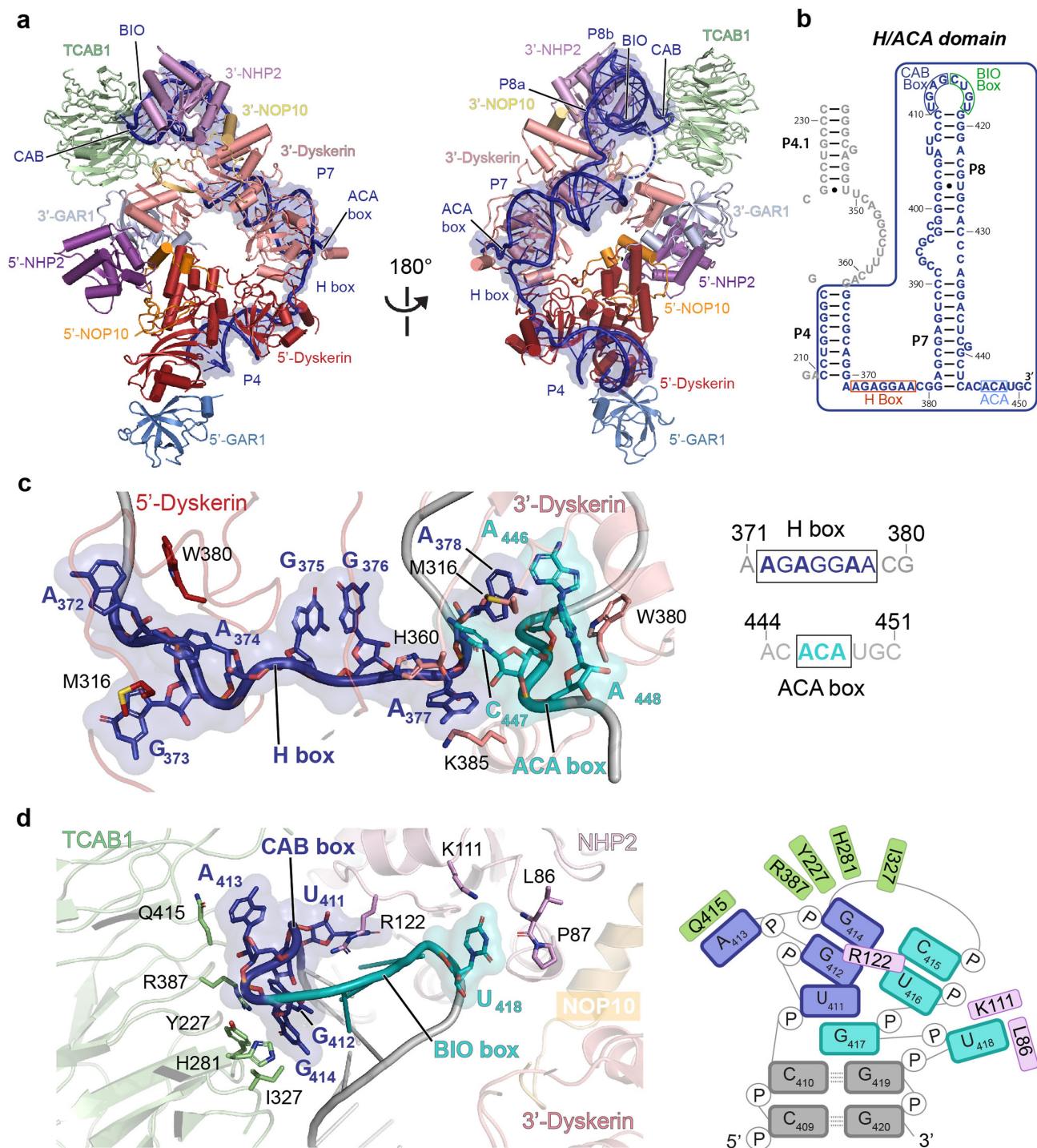
**Extended Data Fig. 8 | H/ACA RNP and molecular interactions of conserved RNA motifs. a**, Front (left) and back (right) views of the H/ACA RNP with subunits coloured as indicated. **b**, Secondary structure schematic of the H/ACA domain of hTR. **c**, Left, close-up view of the H and ACA boxes, and their interactions with each other and with the two dyskerin molecules (Extended Data Figs. 3p, 4k). Right, sequences of H and ACA boxes, with conserved nucleotides highlighted in bold. **d**, Left, close-up view of P8 stem loop and interactions between the CAB and BIO boxes with TCAB1 and NHP2 (Extended Data Figs. 3o, 4l). Right, a schematic of these interactions.

**Extended Data Table 1 | Cryo-EM data collection, refinement and validation statistics**

| | H/ACA lobe EMDB-12177 PDB 7BGB | Catalytic core EMDB-12174 PDB 7BG9 | FL-3D class 2 EMDB-12175 | FL-3D class 5 EMDB-12176 |
|---|---|---|---|---|
| **Data collection and processing** | | | | |
| Magnification | | | | |
| Voltage (kV) | 300 | 300 | 300 | 300 |
| Electron exposure (e$^-$/Å$^2$) | 47 | 47 | 47 | 47 |
| Defocus range (µm) | 1.2-3.2 | 1.2-3.2 | 1.2-3.2 | 1.2-3.2 |
| Pixel size (Å) | 1.11 | 1.11 | 1.11 | 1.11 |
| Symmetry imposed | C1 | C1 | C1 | C1 |
| Initial particle images (no.) | 15,760,434 | 15,760,434 | 15,760,434 | 15,760,434 |
| Final particle images (no.) | 204,665 | 168,538 | 484,847 | 463,013 |
| Map resolution (Å) | 3.40 | 3.81 | 4.53 | 6.63 |
| FSC threshold | 0.143 | 0.143 | 0.143 | 0.143 |
| Map resolution range (Å) | 3.3-7.0 | 3.7-7.0 | 3.9-16 | 4.5-15 |
| | | | | |
| **Refinement** | | | | |
| Initial model used (PDB code) | Ab initio | Ab initio | | |
| Model resolution (Å) | 3.62 | 3.98 | | |
| FSC threshold | 0.5 | 0.5 | | |
| Model resolution range (Å) | 3.3-7.0 | 3.7-7.0 | | |
| Map sharpening $B$ factor (Å$^2$) | -104 | -80 | | |
| Model composition | | | | |
| Non-hydrogen atoms | 14538 | 14233 | | |
| Protein residues | 1574 | 1085 | | |
| Nucleotides | 92 | 262 | | |
| $B$ factors (Å$^2$) | | | | |
| Protein | 232.27 | 206.07 | | |
| Nucleotide | 255.78 | 267.64 | | |
| R.m.s. deviations | | | | |
| Bond lengths (Å) | 0.013 | 0.013 | | |
| Bond angles (°) | 1.591 | 1.620 | | |
| Validation | | | | |
| MolProbity score | 2.37 (99th) | 2.07 (100th) | | |
| Clashscore | 16.5 (97th) | 8.09 (97th) | | |
| Poor rotamers (%) | 0.72 | 0.75 | | |
| Ramachandran plot | | | | |
| Favored (%) | 85.56 | 86.46 | | |
| Allowed (%) | 14.25 | 11.95 | | |
| Disallowed (%) | 0.19 | 1.59 | | |

# Article

**Extended Data Table 2 | Modelling of protein and RNA components**

<table>
<thead>
<tr><th></th><th>Subunit</th><th>Total residues</th><th>M.W. (KDa)</th><th>Modelled</th><th>Chain name</th></tr>
</thead>
<tbody>
<tr><td rowspan="7">Catalytic Core</td><td rowspan="5">TERT</td><td rowspan="5">1132</td><td rowspan="5">127</td><td>TEN: 11-60, 76-100, 125-179</td><td rowspan="5">A</td></tr>
<tr><td>TRBD: 322-415, 444-613</td></tr>
<tr><td>RT: 614-720, 816-951</td></tr>
<tr><td>IFD-TRAP: 721-815</td></tr>
<tr><td>CTE: 952-1132</td></tr>
<tr><td rowspan="2">hTR</td><td rowspan="2">451</td><td rowspan="2">146</td><td>P1 and PK/Template: 26-149, 163-200</td><td rowspan="2">B</td></tr>
<tr><td>CR4/5: 238-248, 251-333</td></tr>
<tr><td>Catalytic Core</td><td>H2A</td><td>130</td><td>14</td><td>18-99</td><td>L</td></tr>
<tr><td></td><td>H2B</td><td>166</td><td>18</td><td>36-125</td><td>M</td></tr>
<tr><td></td><td>DNA</td><td>18</td><td>6</td><td>13-18</td><td>N</td></tr>
<tr><td rowspan="12">H/ACA</td><td>5'-Dyskerin</td><td>514</td><td>57</td><td>36-185, 194-400</td><td>C</td></tr>
<tr><td>5'-GAR1</td><td>217</td><td>21</td><td>70-158</td><td>D</td></tr>
<tr><td>5'-NHP2</td><td>153</td><td>17</td><td>25-152</td><td>E</td></tr>
<tr><td>5'-NOP10</td><td>64</td><td>8</td><td>1-62</td><td>F</td></tr>
<tr><td>3'-Dyskerin</td><td>514</td><td>57</td><td>48-185, 192-392</td><td>G</td></tr>
<tr><td>3'-GAR1</td><td>217</td><td>21</td><td>66-159</td><td>H</td></tr>
<tr><td>3'-NHP2</td><td>153</td><td>17</td><td>25-152</td><td>I</td></tr>
<tr><td>3'-NOP10</td><td>64</td><td>8</td><td>1-64</td><td>J</td></tr>
<tr><td rowspan="3">hTR</td><td rowspan="3">451</td><td rowspan="3">146</td><td>211-218</td><td rowspan="3">B</td></tr>
<tr><td>362-392</td></tr>
<tr><td>397-449</td></tr>
<tr><td rowspan="2">TCAB1</td><td rowspan="2">548</td><td rowspan="2">59</td><td>151-198, 210-317,</td><td rowspan="2">K</td></tr>
<tr><td>325-441, 453-485, 504-510</td></tr>
</tbody>
</table>

# nature research

Corresponding author(s): Thi Hoang Duong Nguyen

Last updated by author(s): 18/02/2021

# Reporting Summary

Nature Research wishes to improve the reproducibility of the work that we publish. This form provides structure for consistency and transparency in reporting. For further information on Nature Research policies, see our Editorial Policies and the Editorial Policy Checklist.

## Statistics

For all statistical analyses, confirm that the following items are present in the figure legend, table legend, main text, or Methods section.

| n/a | Confirmed | |
|---|---|---|
| ☐ | ☒ | The exact sample size ($n$) for each experimental group/condition, given as a discrete number and unit of measurement |
| ☐ | ☒ | A statement on whether measurements were taken from distinct samples or whether the same sample was measured repeatedly |
| ☒ | ☐ | The statistical test(s) used AND whether they are one- or two-sided<br>*Only common tests should be described solely by name; describe more complex techniques in the Methods section.* |
| ☒ | ☐ | A description of all covariates tested |
| ☒ | ☐ | A description of any assumptions or corrections, such as tests of normality and adjustment for multiple comparisons |
| ☐ | ☒ | A full description of the statistical parameters including central tendency (e.g. means) or other basic estimates (e.g. regression coefficient) AND variation (e.g. standard deviation) or associated estimates of uncertainty (e.g. confidence intervals) |
| ☒ | ☐ | For null hypothesis testing, the test statistic (e.g. $F$, $t$, $r$) with confidence intervals, effect sizes, degrees of freedom and $P$ value noted<br>*Give P values as exact values whenever suitable.* |
| ☒ | ☐ | For Bayesian analysis, information on the choice of priors and Markov chain Monte Carlo settings |
| ☒ | ☐ | For hierarchical and complex designs, identification of the appropriate level for tests and full reporting of outcomes |
| ☒ | ☐ | Estimates of effect sizes (e.g. Cohen's $d$, Pearson's $r$), indicating how they were calculated |

*Our web collection on statistics for biologists contains articles on many of the points above.*

## Software and code

Policy information about availability of computer code

| Data collection | Serial-EM 3.7 for cryo-EM data collection |
|---|---|
| Data analysis | The EM softwares were used: Relion 3.1. Structures were built and visualized using Coot 0.8.8, Chimera 1.13.1, ChimeraX 1.0, and Pymol 2.3.2. Gel images were analyzed using ImageJ 1.51. |

For manuscripts utilizing custom algorithms or software that are central to the research but not yet described in published literature, software must be made available to editors and reviewers. We strongly encourage code deposition in a community repository (e.g. GitHub). See the Nature Research guidelines for submitting code & software for further information.

## Data

Policy information about availability of data

All manuscripts must include a data availability statement. This statement should provide the following information, where applicable:
- Accession codes, unique identifiers, or web links for publicly available datasets
- A list of figures that have associated raw data
- A description of any restrictions on data availability

Raw gel source data are provided in Supplementary Fig. 1. Replicates of the activity assays and immunoblotting experiments shown in Fig. 3d and 3e and quantification are included in Supplementary Fig. 2. Full mass spectrometry data and coordinates of hTR from DRRAFTER modeling are provided in Supplementary Information. Cryo-EM maps of the catalytic core, H/ACA lobes and the whole telomerase maps (class 2 and class 5) with both lobes will be deposited with the Electron Microscopy Data Bank under accession number EMD-12174, EMD-12177, EMD-12175, and EMD-12176. Refined atomic coordinates for the catalytic core and H/ACA lobes will be deposited with the Protein Data Bank under accession number PDB-7BG9 and PDB-7BGB. The rigid-body fitted models of the catalytic core and the H/ACA lobes into the whole telomerase maps (class 2 and class 5) are included as a Pymol session in Supplementary videos 5 and 6. The BALBES database was provided internally by the BALBES developers and is available upon request.

# Field-specific reporting

Please select the one below that is the best fit for your research. If you are not sure, read the appropriate sections before making your selection.

☒ Life sciences        ☐ Behavioural & social sciences        ☐ Ecological, evolutionary & environmental sciences

For a reference copy of the document with all sections, see nature.com/documents/nr-reporting-summary-flat.pdf

# Life sciences study design

All studies must disclose on these points even when the disclosure is negative.

| | |
|---|---|
| Sample size | No sample size calculation was made. Cryo-EM data were collected over approximately 9 days until the data yields the number of particles required for extensive classification as described to achieve interpretable maps presented here. |
| Data exclusions | Through 2D and 3D classification procedures, we discarded "bad particles" or classes of particles that did not result in good 3D reconstruction. This procedure is standard in the EM field. |
| Replication | Our native gel shift assays, IPs, activity assays and immunoblotting experiments were performed in three independent replicates, which all showed similar results. We include the replicates in the Supplemental Information. |
| Randomization | Randomization was not relevant to this study because the work did not involve human subjects or live animals. |
| Blinding | Blinding was not relevant to this study because the work did not involve human subjects or live animals. |

# Reporting for specific materials, systems and methods

We require information from authors about some types of materials, experimental systems and methods used in many studies. Here, indicate whether each material, system or method listed is relevant to your study. If you are not sure if a list item applies to your research, read the appropriate section before selecting a response.

### Materials & experimental systems

| n/a | Involved in the study |
|---|---|
| ☐ | ☒ Antibodies |
| ☐ | ☒ Eukaryotic cell lines |
| ☒ | ☐ Palaeontology and archaeology |
| ☒ | ☐ Animals and other organisms |
| ☒ | ☐ Human research participants |
| ☒ | ☐ Clinical data |
| ☒ | ☐ Dual use research of concern |

### Methods

| n/a | Involved in the study |
|---|---|
| ☒ | ☐ ChIP-seq |
| ☒ | ☐ Flow cytometry |
| ☒ | ☐ MRI-based neuroimaging |

## Antibodies

| | |
|---|---|
| Antibodies used | rabbit α-H2A (D603A, clone# 12349, lot 3, 1:250, Cell Signaling Technology, https://www.cellsignal.co.uk/products/primary-antibodies/histone-h2a-d6o3a-rabbit-mab/12349)<br>Rabbit anti-H2B (Ab1790, lot GR3281345-1, 1:1000, Abcam, https://www.abcam.com/histone-h2b-antibody-chip-grade-ab1790.html)<br>Rabbit anti-H3 (Ab1790, lot GR3297885-1, 1:1000, Abcam, https://www.abcam.com/histone-h3-antibody-nuclear-marker-and-chip-grade-ab1791.html)<br>Mouse anti-H4 (L64C1, clone# 2935, lot 6, 1:1000, Cell Signaling Technology, https://www.cellsignal.co.uk/products/primary-antibodies/histone-h4-l64c1-mouse-mab/2935?site-search-type=Products&N=4294956287&Ntt=l64c1&fromPage=plp&_requestid=5790938)<br>Rabbit α-NHP2 (15128-1-AP, 1:1000, Proteintech, https://www.ptglab.com/products/NHP2-Antibody-15128-1-AP.htm)<br>Rabbit α-NOP10 (ab133726, clone# EPR8856, lot YJ021509CS, 1:1000, Abcam, https://www.abcam.com/nop10-antibody-epr8856-ab133726.html)<br>Rabbit α-dyskerin (sc-48794, lot E0214, 1:500, Santa Cruz Biotechnology, https://www.scbt.com/p/dyskerin-antibody-h-300)<br>Rabbit α-Strep (A00626-40, lot 19F001839, 1:500, Genscript, https://www.genscript.com/antibody/A00626-NWSHPQFEK_Antibody_pAb_Rabbit.html).<br>The secondary antibodies used were goat α-rabbit Alexa-Fluor 680 or 790 (ab175773, lot GR222353-8, 1:5000, Abcam, https://www.abcam.com/goat-rabbit-igg-hl-alexa-fluor-680-ab175773.html) and goat α-mouse Alexa-Fluor 680 (ab175775, lot GR3273649-2, 1:5000, Abcam, https://www.abcam.com/goat-mouse-igg-hl-alexa-fluor-680-ab175775.html) |
| Validation | No validation statement could be obtained for the anti-dyskerin antibody. This antibody has been discontinued by the manufacturer, Santa Cruz. All other antibodies have been validated by their manufacturers; the manufacturer's websites stating the validation (including the species and application) of each antibody have been listed above. |

rabbit α-H2A (Cell Signaling)- Western blots of different human cell lysates
rabbit anti-H2B (Abcam)-Western blot against different cell lysates, ChIP data, immunofluorescence data, IP data
rabbit anti-H3 (Abcam)-Western blot against different cell lysates, ChIP data, immunofluorescence data
mouse anti-H4 (Cell Signaling)-Western blot against different cell lysates, immunohistochemistry data
rabbit α-NHP2 (Proteintech)-Western blot against different cell lysates, immunohistochemistry data, immunofluorescence data, IP data
rabbit α-NOP10 (Abcam)-Western blot against different cell lysates, immunohistochemistry data,
rabbit α-Strep (Genscript)-Western blot against Strep-tagged protein
goat α-rabbit Alexa-Fluor 680 or 790 (Abcam)-Western blot against IgG
goat α-mouse Alexa-Fluor 680 (Abcam)-Western blot against IgG

## Eukaryotic cell lines

Policy information about cell lines

| | |
|---|---|
| Cell line source(s) | HEK 293T cells used for protein production were obtained from ATCC® (ATCC® CRL-3216) |
| Authentication | None of the cell lines used were authenticated. This was obtained from a commercial source. |
| Mycoplasma contamination | Cells were not tested for mycoplasma contamination. |
| Commonly misidentified lines (See ICLAC register) | No commonly misidentified lines were used |